

15 JANUARY 1967

GPO PRICE \$ \_\_\_\_\_

CFSTI PRICE(S) \$ \_\_\_\_\_

LMSC-A852904

Hard copy (HC) 306

Microfiche (MF) .65

ff 653 July 65

# STUDY ON HIGH-PERFORMANCE INSULATION THERMAL DESIGN CRITERIA

THIRD QUARTERLY  
PROGRESS REPORT

PREPARED FOR  
GEORGE MARSHALL SPACE FLIGHT CENTER  
HUNTSVILLE, ALABAMA

(THRU) \_\_\_\_\_  
 (CODE) 33 (CATEGORY)  
 (ACCESSION NUMBER) 15757  
 (PAGES) 70  
 (NASA CR OR TMX OR AD NUMBER) C-67456

FACILITY FORM 602

CRYOGENIC STAGE PROGRAMS

LOCKHEED MISSILES & SPACE COMPANY / SUNNYVALE, CALIFORNIA



LMSC-A852904  
15 January 1967

STUDY ON  
HIGH-PERFORMANCE INSULATION  
THERMAL DESIGN CRITERIA

Third Quarterly Progress Report  
Contract NAS 8-20353

Prepared for  
George Marshall Space Flight Center  
Huntsville, Alabama

R. M. Coston  
Program Manager

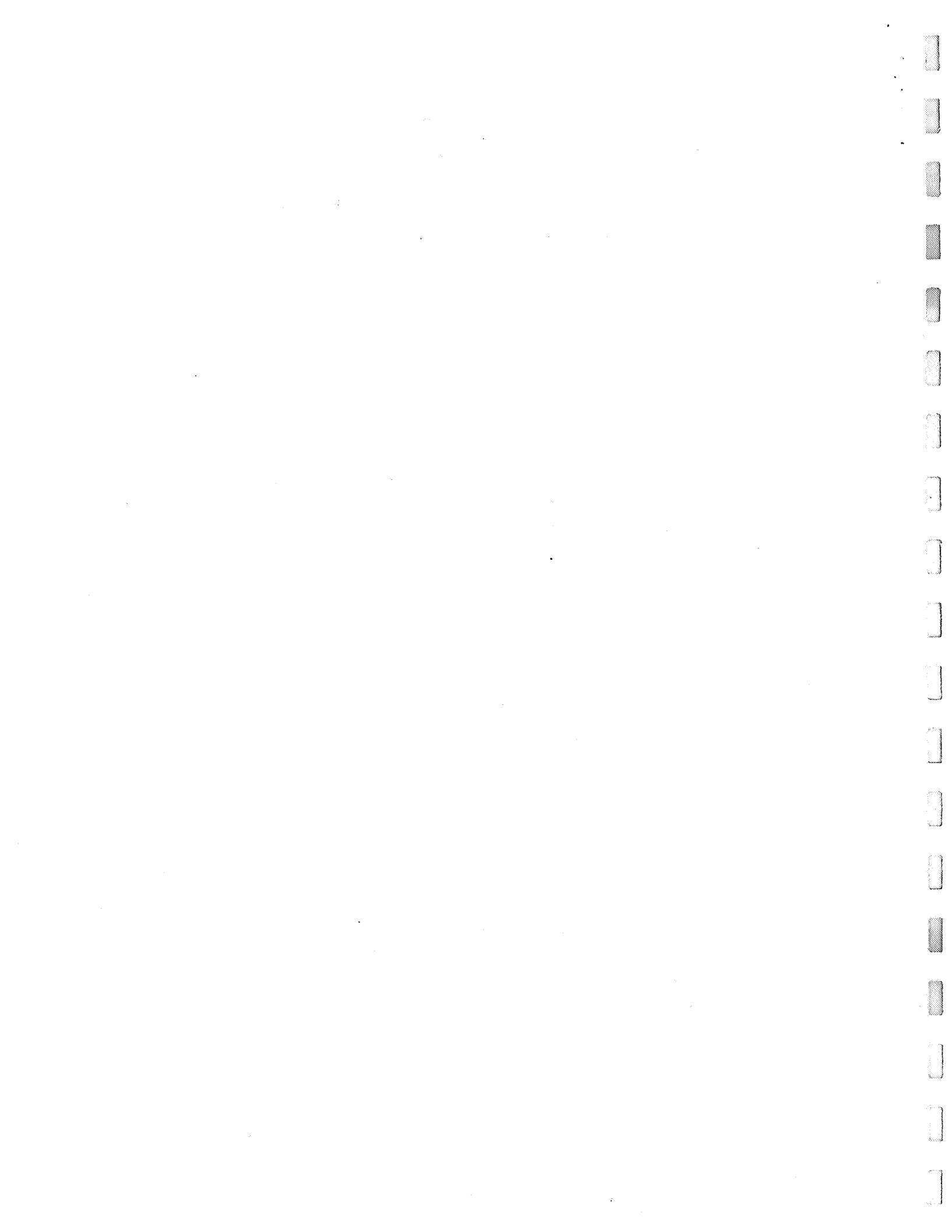
J. J. Brogan, Manager  
Cryogenic Systems

J. H. Guill, Manager  
Cryogenic and Nuclear  
Stage Programs

PRECEDING PAGE BLANK NOT FILMED.

## CONTENTS

	Page
ILLUSTRATIONS	v
TABLES	vii
NOMENCLATURE	ix
SUMMARY	1
PHASE I    COMPUTER PROGRAM CORRELATIONS, REFINEMENTS, AND APPLICATIONS	3
Task 1:    Correlation of CSTM With 82.6-Inch Tank Test Data	3
Task 2A:    Insulation Penetration Studies	15
Task 2B:    Parallel Conductivity of Multilayer Insulations	27
PHASE II    THERMAL DESIGN HANDBOOKS	35
Task 1:    Optical Properties Handbook	35
PHASE III    GAS FLOW STUDIES	39
Task 1:    Outgassing Studies	39
Task 2:    Diffusion Coefficient Study	55
REFERENCES	61



PRECEDING PAGE BLANK NOT FILMED.

## ILLUSTRATIONS

Figure		Page
1	Elements at Tankage System	4
2	CSTM Heat Rate vs Multilayer Thermal Conductivity – 82.6-Inch Tank	5
3	6Al 4V Titanium Thermal Conductivity	7
4	CSTM and Test Heat Rates – 82.6-Inch Tank	9
5	Earth Orbit Insulation Temp. Profiles	10
6	Titanium Cone Temp. Profiles	12
7	CSTM Boiloff Rate vs Multilayer Thermal Conductivity – 82.6-Inch Tank	14
8	Penetration Test Configurations	16
9	Radial Temperature Distribution – LN <sub>2</sub>	19
10	Temperature Distribution Normal to Layers	20
11	Insulation Radial Temperature Distribution, Test 3	21
12	Penetration Assembly	22
13	Penetration and Calibration Apparatus	23
14	Effective Thermal Conductivity of a Double-Aluminized Mylar – Dexiglas Multilayer Insulation System Measured Paralled to the Layers	28
15	Empty Vacuum Chamber Pressure-Rise Characteristics With Dry Air at Ambient Temperature	43
16	Empty Vacuum Chamber Pressure-Rise Characteristics After Being Subjected to 100 Percent Humid Air at Ambient Temperature	44
17	Vacuum Chamber Pressure-Rise Characteristics With Various Insulation Specimens Present at Ambient Temperature After Being Exposed to Dry Air	46
18	Pressure-Rise Characteristics of Vacuum Chamber With and Without Specimen of Crinkled Mylar Aluminized on One Side (NRC-2) at Ambient Temperature and at 140°R	48

Figure		Page
19	Pressure-Rise Characteristics of Vacuum Chamber With and Without Specimen of Aluminum Foil and Dexiglas at Ambient Temperature and 140°R	50
20	Pump-Down Characteristics for Several Off-Shelf Insulation Materials	52
21	Mass Outgassing Rate for Off-Shelf Samples of Multilayer Insulation Materials at Ambient Temperature	54
22	Schematic of Diffusion Apparatus	57
23	Diffusion Apparatus	58
24	Pump-Down Curve for NRC-2 Insulation Sample (Crinkled Single-Aluminized Mylar), 67 Layers/in.	59

## TABLES

Table		Page
1	Penetration Test Schedule	15
2	Effective Thermal Conductivity of a Double-Aluminized Mylar-Dexiglas Multilayer Insulation System Measured Paralled to the Layers	29
3	Schedule of Completed Test Runs	40



PRECEDING PAGE BLANK NOT FILMED.

## NOMENCLATURE

A	Area, integration constant
B	Integration constant
a, b	Equation constants
c	Specific heat of electrons per unit volume
$h_L$	Liquid enthalpy
$h_{ve}$	Vapor enthalpy at vent inlet
k	Thermal conductivity
L	Length
l	Mean free part of electrons
$\dot{m}$	Mass boiloff rate of hydrogen
P	Pressure
$Q_c$	Heat flux to the cryogen
$Q_H$	Heater power
$Q_{ins}$	Heat flux through the insulation
$Q_L$	Thermal link heat flux
$Q_o$	Volumetric outgassing rate
$Q_P$	Sum of heater power
$Q_{RAD}$	Radiation heat flux
$Q_s$	Sample of outgassing rate
$Q_X$	Heat transfer rate between insulation and penetration
T	Temperature
$T_c$	Cold boundary temperature
$T_H$	Hot boundary temperature
t	Time
V	Volume
v	Velocity of electrons
$\epsilon$	Total hemispherical emittance
$\alpha_s$	Solar absorptivity

## SUMMARY

The correlation of the Complete System Thermal Model (CSTM) computer program predictions with the 82.6-inch tank test data was completed during this reporting period. CSTM predictions ranged from 16 to 34 percent lower than test data depending on the interpretation of ullage gas superheat test data. This correlation is based on cryostat data of insulation specimens which indicated an effective thermal conductivity of  $3.6 \times 10^{-5}$  Btu/hr-ft  $^{\circ}$ R. A parametric study conducted with the CSTM to determine the effect of insulation system thermal conductivity on the effectiveness of the 82.6-inch tank thermal protection system shows a correlation between test data and predictions at conductivities ranging from  $5.2 \times 10^{-5}$  Btu/hr-ft  $^{\circ}$ R to  $8.6 \times 10^{-5}$  Btu/hr-ft  $^{\circ}$ R depending again on the value of ullage gas superheat chosen.

During this reporting period further experimental data were obtained in the continuing investigation of heat transport occurring in and around multilayer insulation penetrations. Further data are presented on the insulation performance without penetration. These data indicate that gas was not trapped within the multilayer interstices in a previous test. Additionally, data are presented on the insulation response to the initial penetration configuration. Results show a significant change in the system performance.

The final measurements of the effective parallel thermal conductivity of a specimen of double-aluminized Mylar-Dexiglas insulation were made. The most recent data were obtained with a specimen length of 3.4 inches to determine the effect of radiation tunneling through this particular type of insulation. It was concluded that radiation tunneling is not significant in this insulation. Also in this reporting period a test specimen of NRC-2 insulation was fabricated and installed in the parallel conductivity cryostat. Data were obtained for this specimen with boundary temperature at 252 $^{\circ}$ R and 540 $^{\circ}$ R. These results indicate a large amount of radiation tunneling present.

Analyses were conducted to evaluate the temperature dependence of parallel conductivity in the multilayer insulation. The deviation of thin film behavior from the bulk material behavior is a result of confining the aluminum free electron motion by the boundaries of the aluminum film. The electron mean free path in the aluminized layer is invariant with temperature, for the temperature range tested, because the film thickness is smaller than the mean free path predicted from kinetic theory based on the material temperature. The net result is that the thermal conductivity is a linear function of temperature.

Work has been initiated on the Optical Properties Handbook, and during this reporting period efforts were directed to defining requirements and organization of material. An outline of the handbook is presented and described. A preliminary draft was prepared on Lockheed Research Coating Systems for inclusion in the Optical Properties Handbook. Additional sections have been partially completed.

The bulk of the outgassing testing was completed during this reporting period. Due to the sorptive characteristics of the various insulation materials it was found necessary to abandon the originally proposed method of data acquisition in favor of a new approach, in which the outgassing rate is determined from comparison of the vacuum chamber pumpdown characteristics when empty and with an insulation specimen present. Data are presented from both techniques. Outgassing rates have been determined for "off the shelf" specimens of Dexiglas, double aluminized Mylar, crinkled single-aluminized Mylar, and aluminum foil at ambient temperatures.

The flowmeter required for the diffusion coefficient studies was constructed and calibrated during this reporting period. In this reporting period it was found necessary to increase the pumping speed of the vacuum system of the apparatus in which the diffusion coefficients are determined. These modifications were completed and a test specimen of NRC-2 insulation was installed in the apparatus for measurement of its diffusion coefficient.

## PHASE I. COMPUTER PROGRAM CORRELATIONS, REFINEMENTS AND APPLICATIONS

### TASK 1: CORRELATION OF CSTM WITH 82.6-INCH TANK TEST DATA

Correlation of CSTM predictions and 82.6-inch tank test data was completed during this reporting period. Included in the correlation is a parametric study conducted to establish the overall system thermal sensitivity to the multilayer insulation effective thermal conductivity. A detailed analysis of CSTM predictions together with test data is being documented to be included in the final report. A summary of this correlation is included in this activity report.

In the CSTM mathematical mockup of the 82.6-inch tank and thermal protection system the tank and insulation systems were divided into five major elements. The shroud was divided into three major elements. All elements are shown in Figure 1. Element 1 is the top fiberglass cover and element 2 the bottom fiberglass cover. These elements include the intermediary fiberglass mat which separates the cover insulation systems from the spherical sector insulation system of elements 4 and 5. Element 3 is the conical support and a portion of the tank wall between the upper spherical section 4 and bottom spherical sector 5. Element 6 is the shroud, and elements 7 and 8 are further divided into three sections circumferentially. The elements shown were divided into a total of 1,200 nodes for the analogous electrical network.

Figure 2 shows the heat rates predicted by the CSTM for a range of multilayer thermal conductivities perpendicular to the layers from  $3 \times 10^{-5}$  to  $12 \times 10^{-5}$  Btu/hr-ft  $^{\circ}$ R. These data apply to the simulated earth-orbit environment in the steady-state. The predicted heat rates through the elements identified in Figure 1 are also shown. The heat rate through element 1 amounts to 8 percent of the total at the lowest conductivity value and decreases to 7 percent of the total at the highest conductivity value studied. The heat rate through element 2 is 7 percent of the total at the lowest conductivity value and 6 percent at the highest value. The heat rate through element 3 decreases from

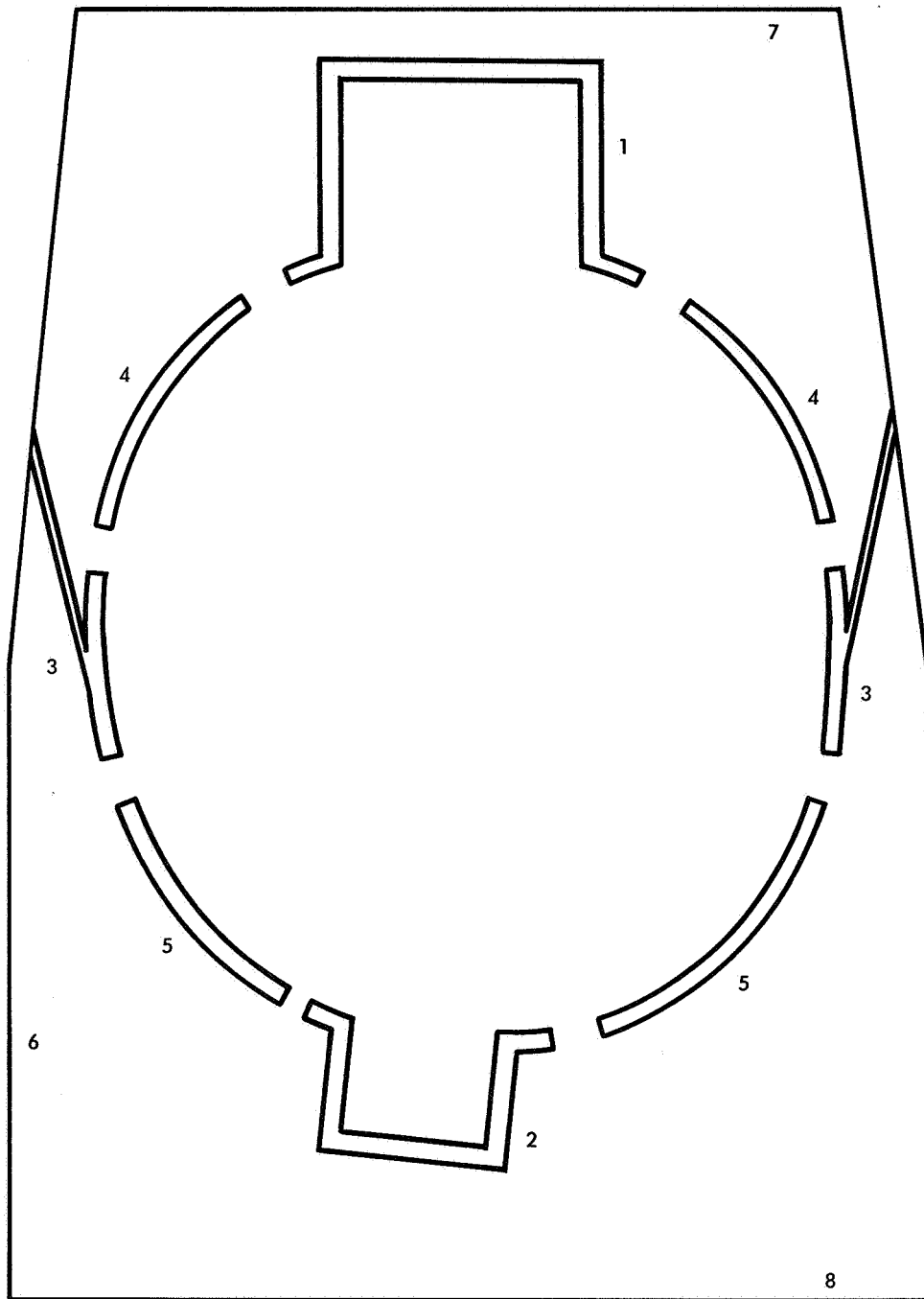


Fig. 1 Elements at Tankage System

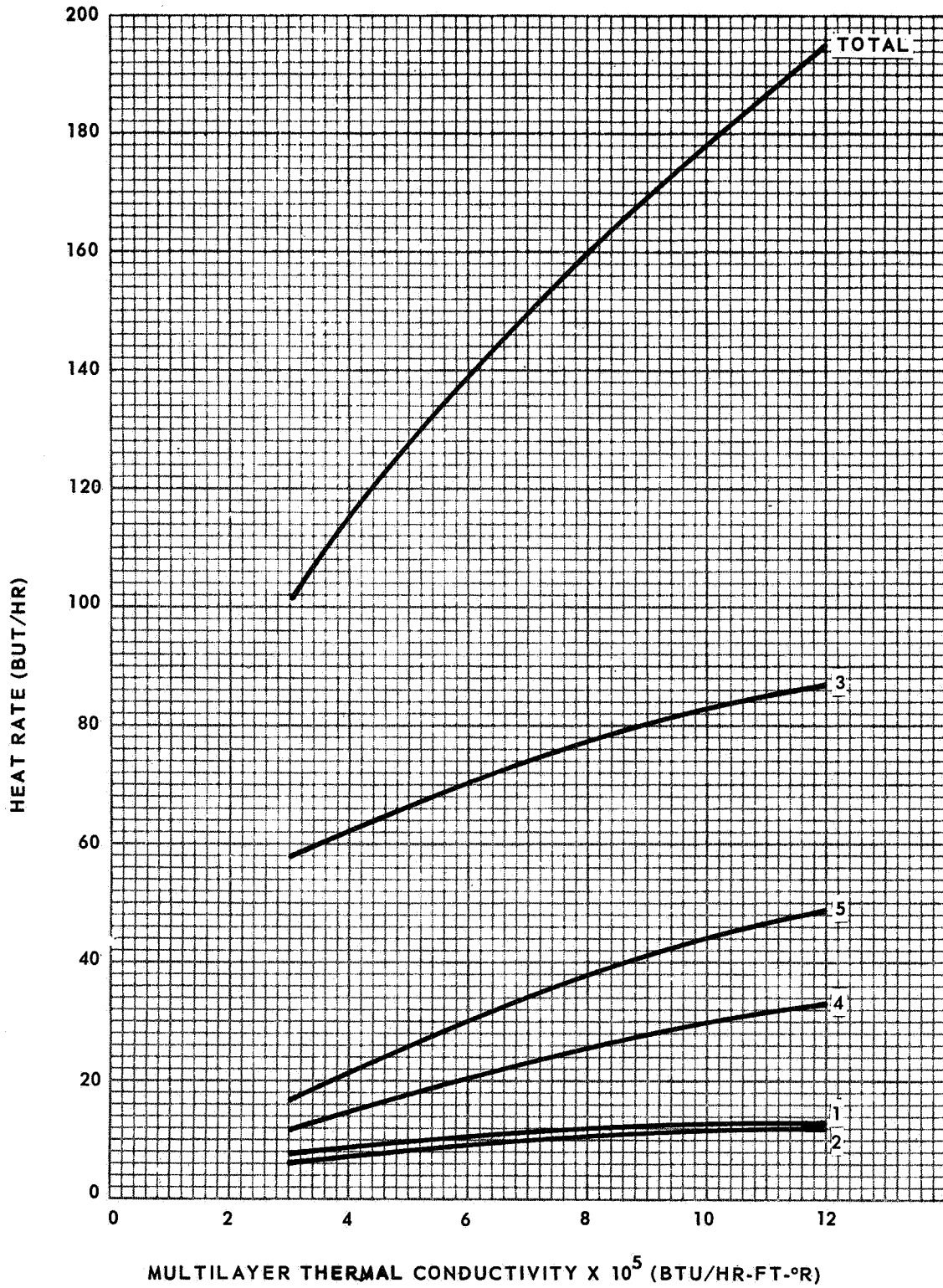


Fig. 2 CSTM Heat Rate vs Multilayer Thermal Conductivity - 82.6-Inch Tank

57 to 45 percent from the lowest to the highest conductivity, the element 4 heat rate increases from 11 to 17 percent, and element 5 heat rate increases from 17 to 25 percent in going from the lowest to highest conductivity values.

#### Data Evaluation

The measured hydrogen boiloff rate was used to calculate the total heat rate passing through the thermal protection system and reaching the LH<sub>2</sub>. The relationship used was:

$$Q = \dot{m} (h_{ve} - h_L)$$

where

- $\dot{m}$  = mass boiloff rate of hydrogen
- $h_{ve}$  = vapor enthalpy at vent inlet
- $h_L$  = liquid enthalpy

In order to determine the vapor enthalpy at the vent inlet, the gas temperature at this location must be known in addition to the pressure. The vent gas enthalpy at the vent inlet may not necessarily be that of saturated vapor; it could be superheated because of energy exchanges with the tank wall. To determine whether ullage gas superheating occurred during the 82.6-inch tank tests, two platinum resistance thermometers (RTB-8 and RTB-16) were placed in the ullage volume. RTB-8 was suspended 6.7 inches from the inlet of the vent line while RTB-16 was attached to the outside top of the tank at a location 1.5 inches from the side of the vent line. The true temperature and enthalpy of the effluent vapor at the vent inlet lies between the temperature measurements at RTB-8 and RTB-16. The measured boiloff rate under the simulated earth-orbit environment was 0.69 lb/hr. The corresponding calculated heat rates for a no-superheat condition, superheat based on RTB-8 calculation, and superheat based on RTB-16 calculation are 131, 140 and 166 Btu/hr, respectively. The solid conduction heat leaks through the plumbing lines, conical support, and fiberglass covers vary from 14 to 18 percent of the total depending on which superheat value is used. The calculated head leak through the titanium cone based on the conductivity of Figure 3 amounts to approximately 60 percent of the total solid conduction heat leak or about 9 to 11 percent of the total heat leak.

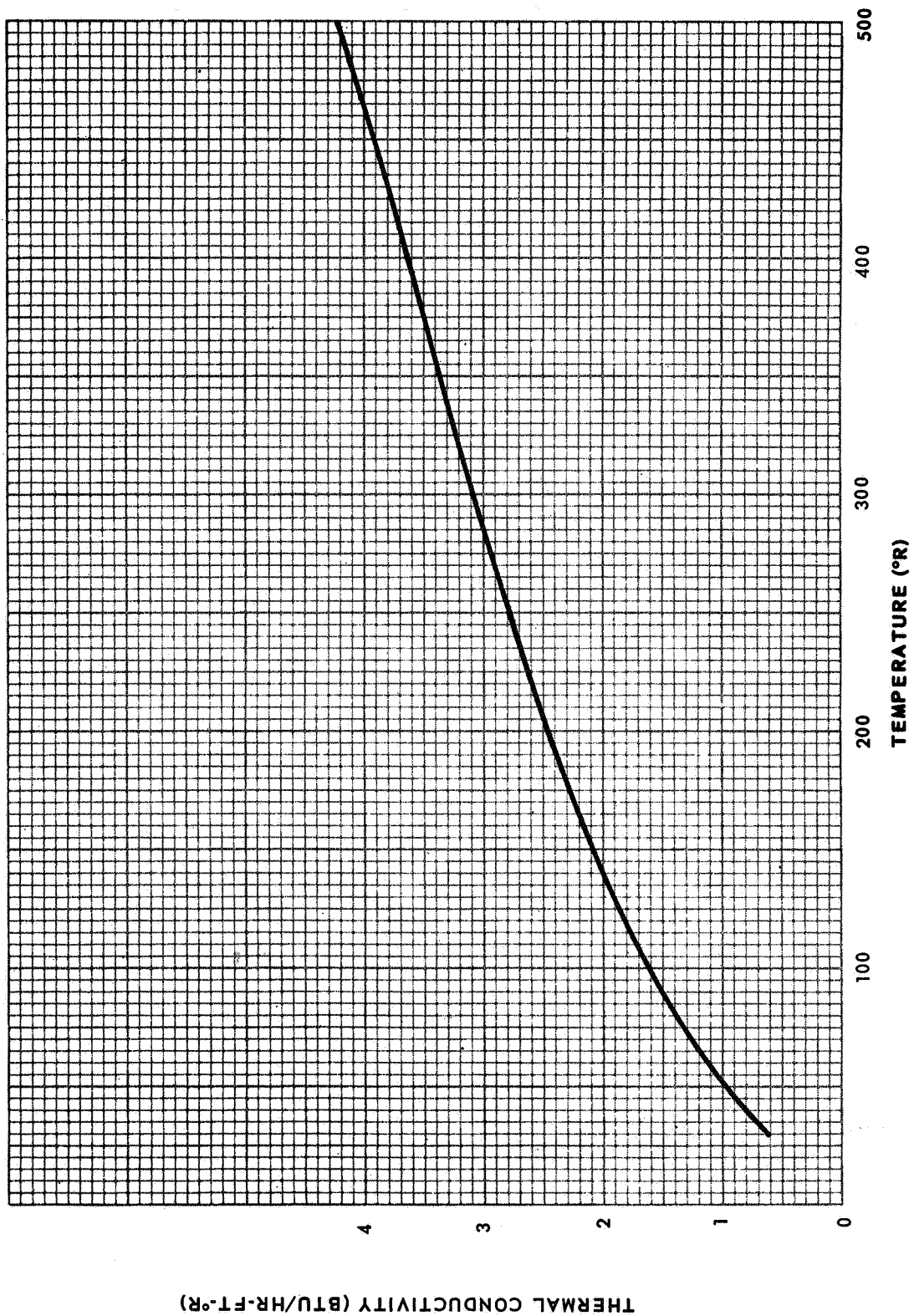


Fig. 3 6AL 4V Titanium Thermal Conductivity

### Data and CSTM Correlation

Figure 4 again shows the total heat input predicted by the CSTM and additionally shows the test results for the two superheat conditions and the no-superheat condition. Cryostat tests indicate a value of multilayer conductivity perpendicular to the layers of approximately  $3.6 \times 10^{-5}$  Btu/hr-ft  $^{\circ}$ R. Using this value the CSTM predicts a total heat rate of 110 Btu/hr. The test results are approximately 16 percent higher than the value for the no-superheat condition, 22 percent higher for the RTB-8 superheat calculation, and 34 percent higher for the RTB-16 superheat calculation. To correlate with the no-superheat condition the conductivity would have to be  $5.2 \times 10^{-5}$  Btu/hr-ft  $^{\circ}$ R. Correlation with the RTB-8 superheat test condition would require a conductivity of  $6 \times 10^{-5}$  Btu/hr-ft  $^{\circ}$ R, and correlation with the RTB-16 superheat test condition would require a conductivity of  $8.6 \times 10^{-5}$  Btu/hr-ft  $^{\circ}$ R. The discussion of the correlation is based on the RTB-8 superheat test condition using a multilayer conductivity of  $6 \times 10^{-5}$  Btu/hr-ft  $^{\circ}$ R.

The temperature profiles through the multilayer insulation at four locations are shown in Figure 5. The CSTM temperature profile is also shown for comparison. The temperature measurement locations are presented as a function of the ratio of the number of multilayers to the total number of multilayers since the absolute location of the thermocouples within the insulation is not precisely known. The average total temperature difference across the multilayers is  $275^{\circ}$ R for the test case compared to  $282^{\circ}$ R predicted using the CSTM. The average temperature difference across the sublayer for the test data is  $67^{\circ}$ R compared to  $57^{\circ}$ R for the CSTM prediction. The calculated heat flux through the sublayer from the test data is  $.458 \text{ Btu/ft}^2\text{-hr}$  based on an average thickness of .54 inch, an average temperature difference of  $67^{\circ}$ R, and a conductivity of  $30.8 (10)^{-5} \text{ Btu/ft-hr } ^{\circ}$ R. The calculated heat flux through the sublayer for the CSTM case is  $.509 \text{ Btu/ft}^2\text{-hr}$  based on a thickness of .40 inch, a temperature difference of  $56.6^{\circ}$ R and a conductivity of  $30 (10)^{-5} \text{ Btu/ft-hr } ^{\circ}$ R. The predicted heat flux obtained from the CSTM is approximately 11 percent higher than the value calculated for the test data.

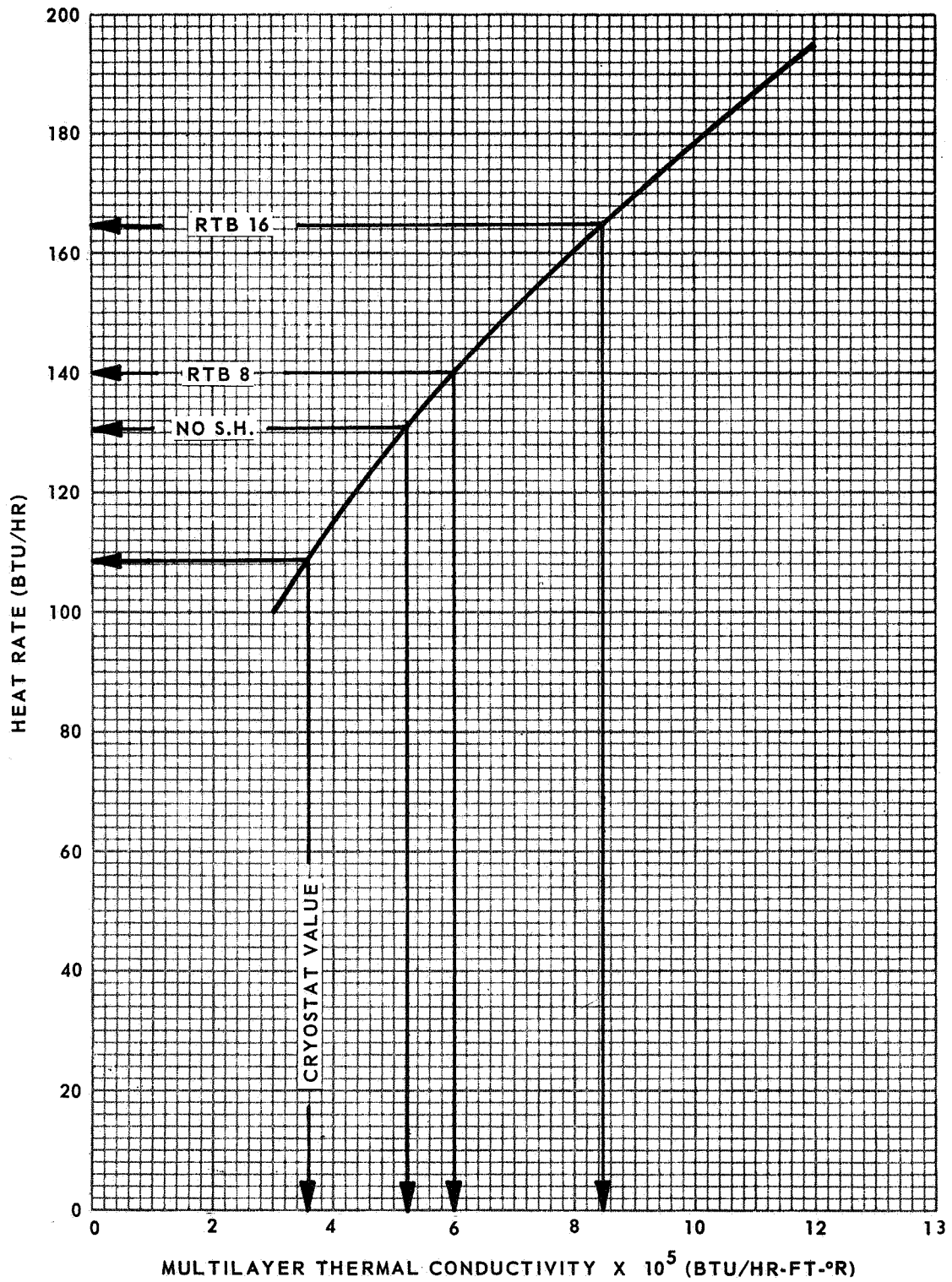


Fig. 4 CSTM and Test Heat Rates - 82.6-Inch Tank

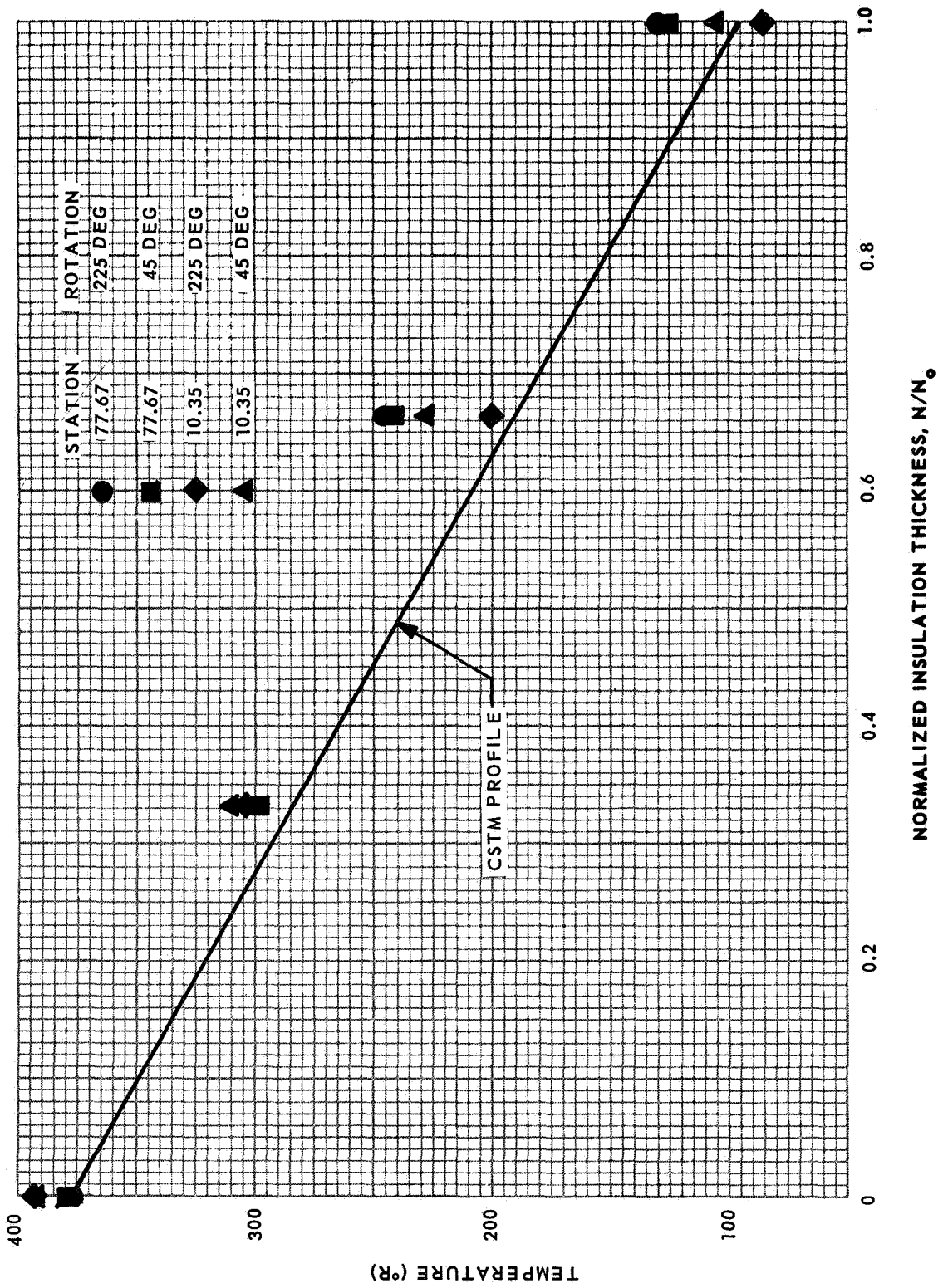


Fig. 5 Earth Orbit Insulation Temp. Profiles

The calculated thermal conductivity of the multilayers is equal to  $15 (10)^{-5}$  Btu/hr-ft  $^{\circ}$ R if the heat flux through the layers is assumed to be the same as across the sublayer which is .458 Btu/ft<sup>2</sup>-hr. The average values of temperature differential and thickness of 277 $^{\circ}$ R and 1.1 inches, respectively, were used to obtain this flux. However, since the multilayer thickness was assumed to be the difference between the total thickness and sublayer thickness, the value of 1.1 inches is probably greater than the actual thickness. The multilayers system is attached to the purge bag with Velcro fasteners that serve as standoffs and add to the total thickness. On the bottom portion of the tank, the insulation is free to sag between the Velcro fasteners, adding to the measured total thickness. Also, since the sublayer thickness was measured after the multilayer system was removed, it is possible that the sublayer thickness on the bottom was actually larger when the multilayer system weight was being supported. When such uncertainty exists in the actual thickness to be used it is more meaningful to compare the thermal resistivities. For the test data the multilayer thermal resistivity is equal to 600 ft<sup>2</sup>-hr  $^{\circ}$ R/Btu based on the sublayer heat flux of 0.458 Btu/ft<sup>2</sup>-hr and the temperature gradient of 277 $^{\circ}$ R. The CSTM multilayer thermal resistivity is equal to 555 ft<sup>2</sup>-hr  $^{\circ}$ R/Btu or about 8 percent lower than the test data.

The conical section shown as element 3 on Figure 1 includes the conical support insulation around the tank circumference. The CSTM results indicate that 50 percent (70.2 Btu/hr) of the heat entering the tank passes through this section. The insulation in this section is "shorted out" by the titanium cone and the fiberglass strips around the tank that separate the cone insulation from the bottom and top spherical sector insulation systems. The temperature gradient at the outer surface of the bottom strip is 174.5 $^{\circ}$ R/inch as predicted by the CSTM. This results in a heat rate of 11.5 Btu/hr or 16 percent of the total heat rate into the element. The temperature gradient at the outer surface of the top strip is 122 $^{\circ}$ R/inch. This results in a heat rate of 7.2 Btu/hr or 10 percent of the total into the element.

The CSTM predicted heat rate due to solid conduction along the titanium cone is 22.4 Btu/hr or 32 percent of the total into the element. The measured test heat rates were 16.2 Btu/hr at 45-degree rotation and 12.6 Btu/hr at 225-degree rotation. Figure 6 compares the cone temperature distributions for the CSTM predictions and

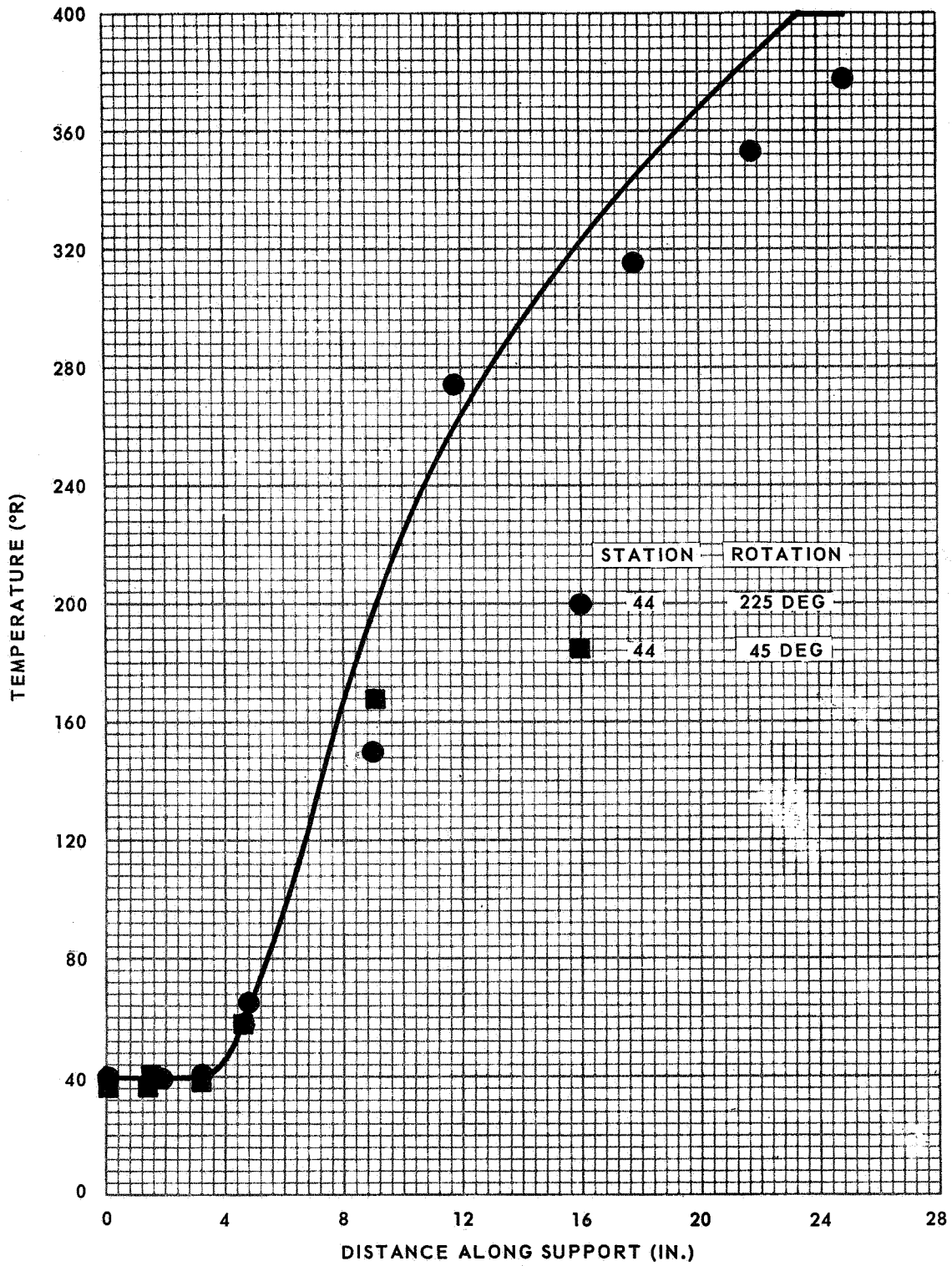


Fig. 6 Titanium Cone Temp. Profiles

test data. The remaining heat into the element enters through the multilayers and comprises 42 percent of the total (29.5 Btu/hr) into the element. If this element were covered with the insulation system without any penetrations or fiberglass strips, the CSTM would predict a heat input of 27.7 Btu/hr.

The remaining 14 percent of the total heat input into the tank enters through the top and bottom covers designated as elements 1 and 2 on Figure 1. It is interesting to note that if the superheat considerations are neglected and the correlation is based on boil-off rate rather than heat rates, the CSTM predicts 0.58 lb/hr which is 16 percent lower than the measured value of 0.69 lb/hr. These results are shown on Figure 7. Since it is the boiloff rate that is of interest when evaluating an insulation system for a particular vehicle-mission combination, the CSTM would predict a boiloff about 16 percent lower than actual.

Application of a multilayer insulation system to a tank probably results in some degradation of the insulation effectiveness because of local compressions and expansions of the layers, effects of joints, fasteners, and penetrations. It seems possible that the difference in conductivity between the cryostat value and that needed to obtain correlation could be due to these effects.

Insulation gaps at joints tend to raise the thermal conductivity of the insulation. A test specimen consisting of double aluminized 1/4-mil Mylar and of alternate layers of Dexiglas spacer material was tested with and without a gap to determine the effect of gap width on the thermal conductivity of the insulation. The thickness was 0.535 inch, and the layer density was 65.5 layers per inch. The thermal conductivity without a gap was  $1.99 (10)^{-5}$  Btu/ft-hr  $^{\circ}$ R with a warm boundary temperature of  $530^{\circ}$ R and a cold boundary temperature of  $139^{\circ}$ R. The test specimen was then cut in half and the resulting gap was covered with a double-aluminized Mylar sheet 4 inches wide placed over the gap. With a 1/16-inch gap the conductivity increased by 11.5 percent; with a 1/8-inch gap the conductivity increased by 43.7 percent; and with a 1/4-inch gap the conductivity increase was 95 percent. It is difficult to assess what the effect would be due to the gaps at the insulation joints on the 82.6-inch diameter tank. However, it results in an increase in the reference thermal conductivity value obtained from cryostat tests. The value of  $k = 6 (10)^{-5}$  Btu/hr-ft $^{\circ}$ R needed to correlate the test data would appear to be a reasonable value for the insulation system on the 82.6-inch tank.

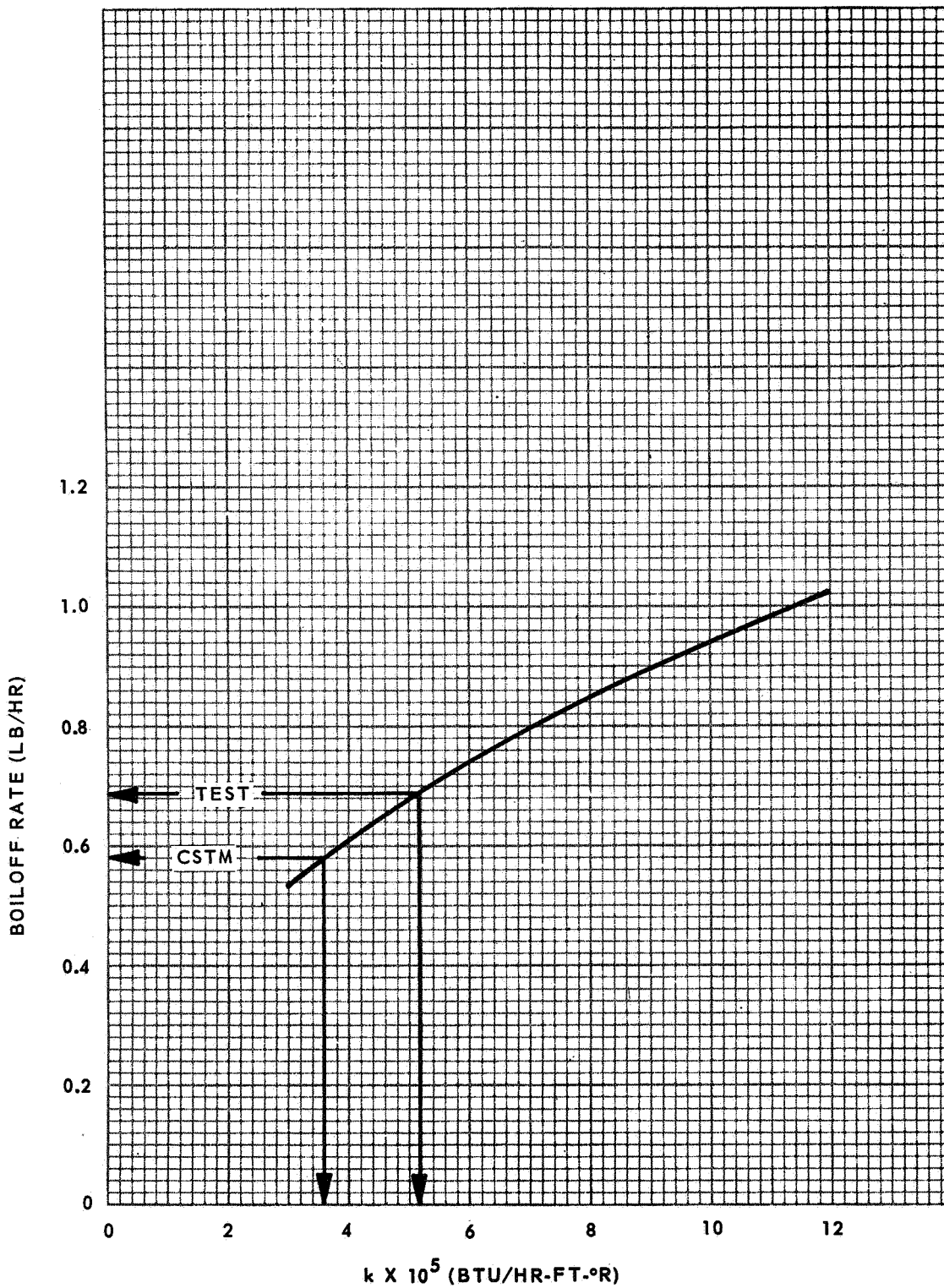


Fig. 7 CSTM Boiloff Rate vs Multilayer Thermal Conductivity - 82.6-Inch Tank

## TASK 2A: INSULATION PENETRATION STUDIES

During this third quarterly reporting period, further experimental data were obtained in the continuing investigation of heat transport occurring in and around multilayer insulation penetrations. Additional information was obtained on the insulation performance with no penetration. After establishing the baseline (no penetration) performance, the insulation response to the initial penetration configuration was evaluated. The penetration assembly utilized in these tests was fabricated and partially calibrated during this reporting period.

A schedule of all tests to be conducted in this phase of the program, including those already completed, are shown in Table 1. The penetration configurations referred to in Table 1 are shown in Figure 8. To date Tests 1 through 5 have been completed and Test 6 is in progress.

Table 1  
PENETRATION TEST SCHEDULE

<u>Start Date</u>	<u>Test</u>	<u>Test Config.</u>	<u>Cryogen</u>	<u>Penetration Dia. (in.)</u>	<u>Intermediary Dia. (in.)</u>	<u>Approximate Penetrant Temp. Grad. (°R/in.)</u>
9/25/66	1	1	LN <sub>2</sub>	0	—	—
10/25/66	2	1-a	LN <sub>2</sub>	0	—	—
10/30/66	3	1-a	LN <sub>2</sub>	0	—	—
12/12/66	4	2	LN <sub>2</sub>	1	0	0, 46, 91
12/19/66	5	2	LN <sub>2</sub>	1	0	0, 91
1/16/67	6	3	LN <sub>2</sub>	1	3	0, 46, 91
1/30/67	7	4	LN <sub>2</sub>	1	6	0, 91
2/ 6/67	8	5	LN <sub>2</sub>	1	6	0, 91
2/20/67	9	6	LN <sub>2</sub>	1	6	0, 91

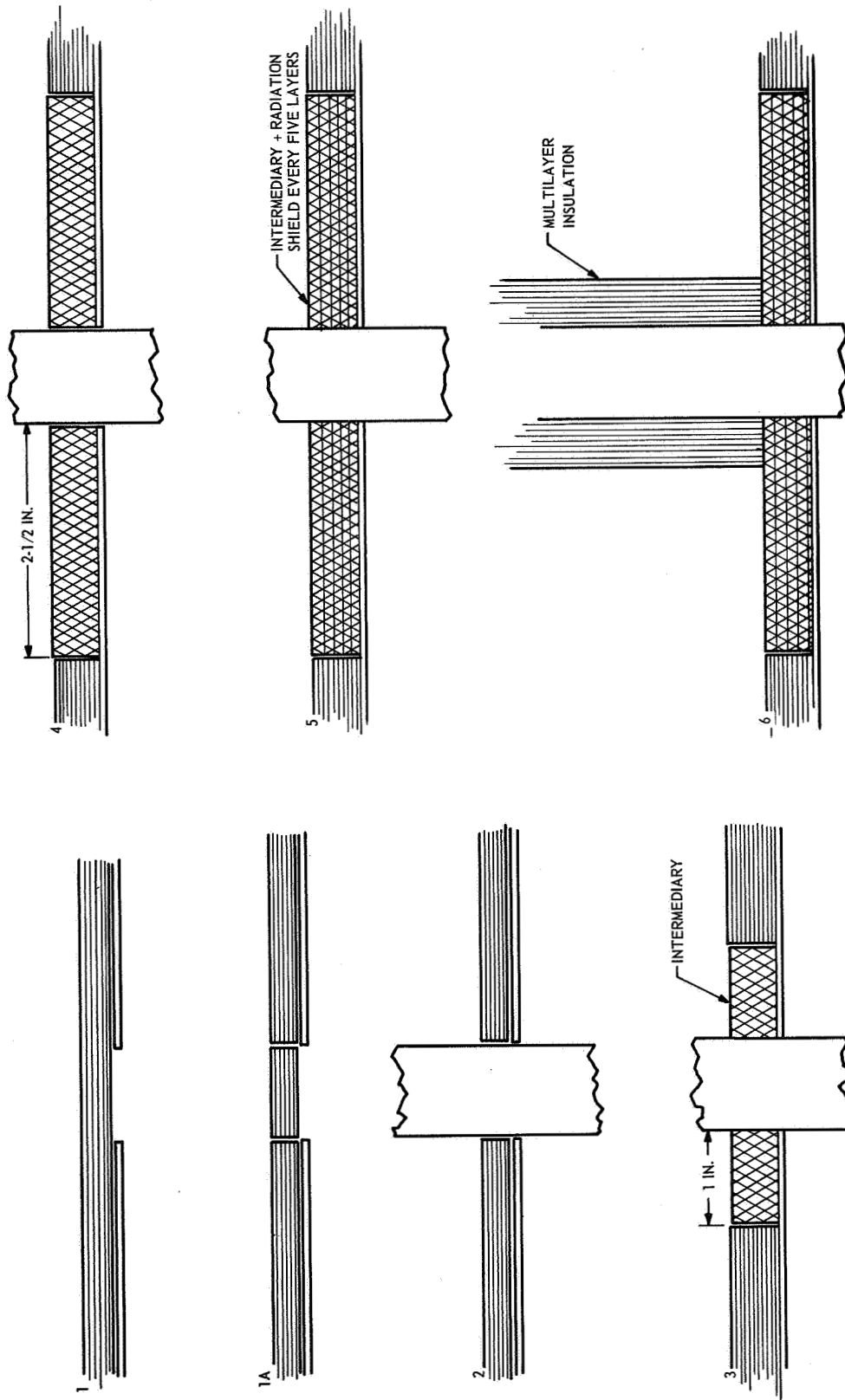


Fig. 8 Penetration Test Configurations

Tests 2 and 3

During the previous reporting period, insulation thermal performance tests were conducted on the penetration cryostat to establish an insulation baseline performance (Test 1). The resultant heat flow through the insulation for these tests was reported as  $0.6 \text{ Btu/hr-ft}^2$  with a corresponding effective thermal conductivity of  $9.0 \times 10^{-5} \text{ Btu/hr-ft}^{\circ}\text{R}$  based on an insulation thickness of 0.7 inch. However, in view of the higher-than-expected apparent thermal conductivity, there was some question concerning the origin of the higher thermal conductivity. Temperature profiles along the 10th and 40th insulation layers led to the conclusion that a higher layer density at the edges of the cryostat were responsible for the higher heat rates. However, there was also the possibility that due to the insulation configuration the insulation interstices were not completely evacuated below  $10^{-4}$  torr. This would result in a higher heat rate through the insulation. To fully resolve the problem, it was decided that another experiment (Test 2) would be conducted in which a hole the size of the initial penetration (1-1/8-inch dia.) would be cut in the center of the insulation, thereby providing a shorter diffusion path for the gas molecules within the insulation. Further, to avoid a substantial increase in heat rate to the cryogen, a plug of multilayer insulation was inserted into the hole, leaving a gap of approximately 1/32 inch between the plug and the main body of insulation.

After cutting the hole in the insulation, the thickness of the insulation was checked and found to be 0.5 inch as compared to the originally reported 0.7 inch. It is felt that the value of 0.5 inch is more representative of the insulation thickness, as previous dimensions were not obtained directly but were inferred from external measurements. This, together with flow meter calibration data, would reduce the previously reported value of effective thermal conductivity to  $5.6 \times 10^{-5} \text{ Btu/hr-ft}^{\circ}\text{R}$  for a layer density of 100 layers per inch.

The results of Test 2 show a three percent decrease in the heat flux to the  $\text{LN}_2$  for a value of  $0.48 \text{ Btu/hr-ft}^2$ . Since this is within the measuring accuracy of the flow meter, it is concluded that if there were gas molecules entrapped within the insulation, then their effective pressure was too low to affect the heat rate through the insulation.

During the initial evacuation of the cryostat in Test 1, it was observed that the insulation on the penetration cryostat dilated and contracted. This led to the question of dimensional stability of the insulation between the one-atmosphere condition and the fully evacuated condition. In the latest series of tests a cathetometer was set up to observe these dimensional changes through a glass port in the vacuum chamber. The cathetometer has a measurement accuracy of 0.001 inch. During the very first phases of evacuation the insulation was observed to billow out considerably; but after complete evacuation, it was found that the insulation returned to its original one-atmosphere measured thickness of 0.5 inch.

The temperature data obtained in Test 2 were very similar in slope to that previously measured in Test 1 and are shown for comparison in Figure 9. . However, the temperature level is seen to be lower for Test 2. The temperature distribution normal to the insulation layers is shown in Figure 10.

Upon completion of the tests with  $\text{LN}_2$  as the heat sink, the residual  $\text{LN}_2$  was removed by blowing warm helium gas through the cryostat. The cryostat was then filled with  $\text{LH}_2$ , and the system was allowed to reach equilibrium from  $\text{LN}_2$  temperatures. The data for Test 3 were then obtained. The measured heat flux through the insulation is  $0.53 \text{ Btu/hr-ft}^2$  yielding an effective thermal conductivity of  $4.5 \times 10^{-5} \text{ Btu/hr-ft } ^\circ\text{R}$ . The measured temperature gradients, both normal and parallel to the layers, are presented in Figures 10 and 11, respectively. These data are as expected.

#### Penetration Assembly

The penetration assembly utilized in Tests 3 and 4 is shown in the schematic of Figure 12 and the photograph of Figure 13. The platinum resistance thermometer is a four-lead, 500-ohm element with  $\pm 1^\circ\text{F}$  capability. This thermometer will be used as the fixed-temperature point to reference the penetration thermocouple (T.C.-P). This gold-cobalt (Au: 2.1 at. % Co) differential thermocouple will measure the temperature of the one-inch O.D. by .010-inch wall stainless steel (Type 347, full annealed) penetration at the top layer of multilayer insulation.

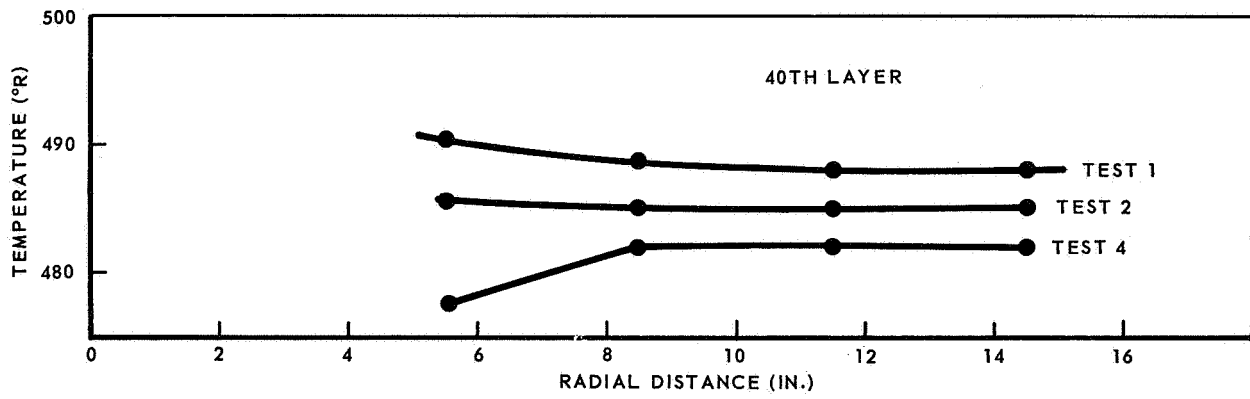
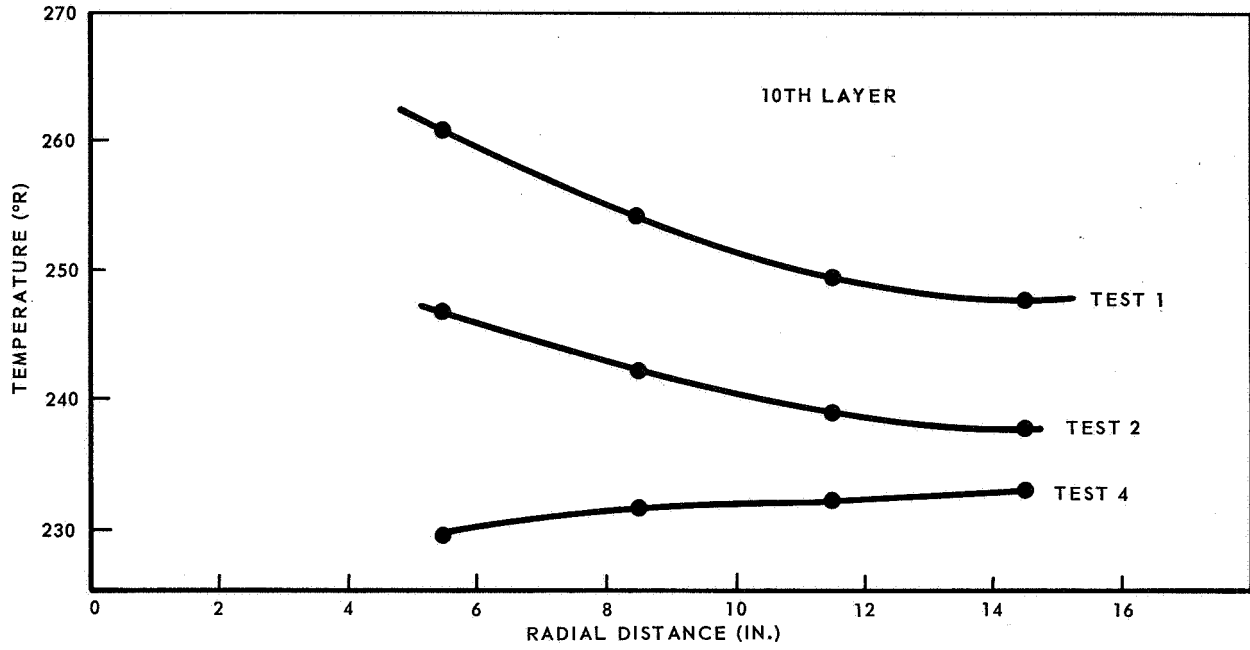


Fig. 9 Radial Temperature Distribution - LN<sub>2</sub>

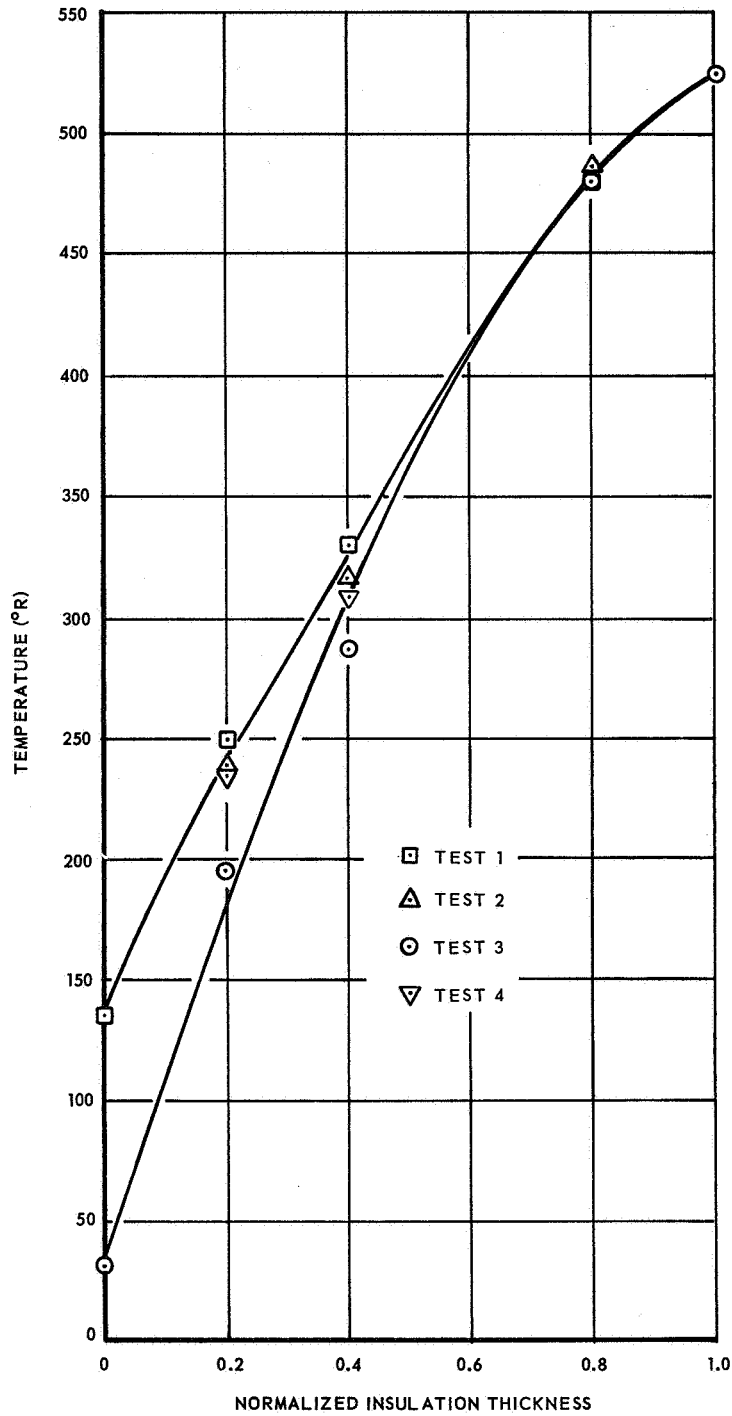


Fig. 10 Temperature Distribution Normal to Layers

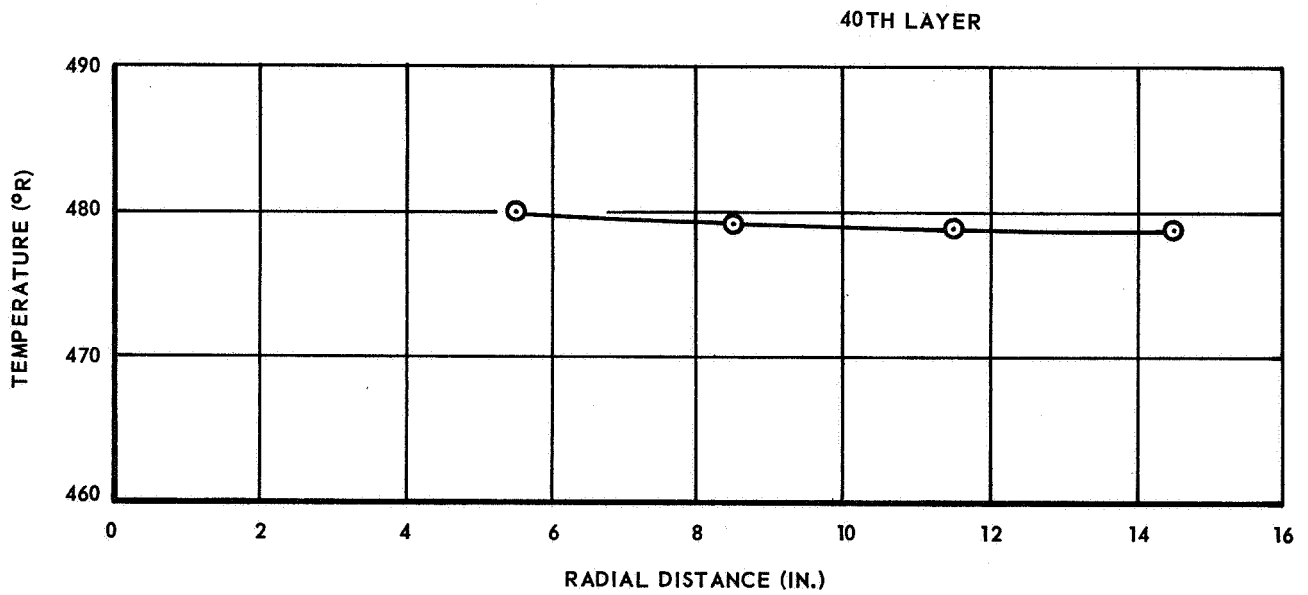
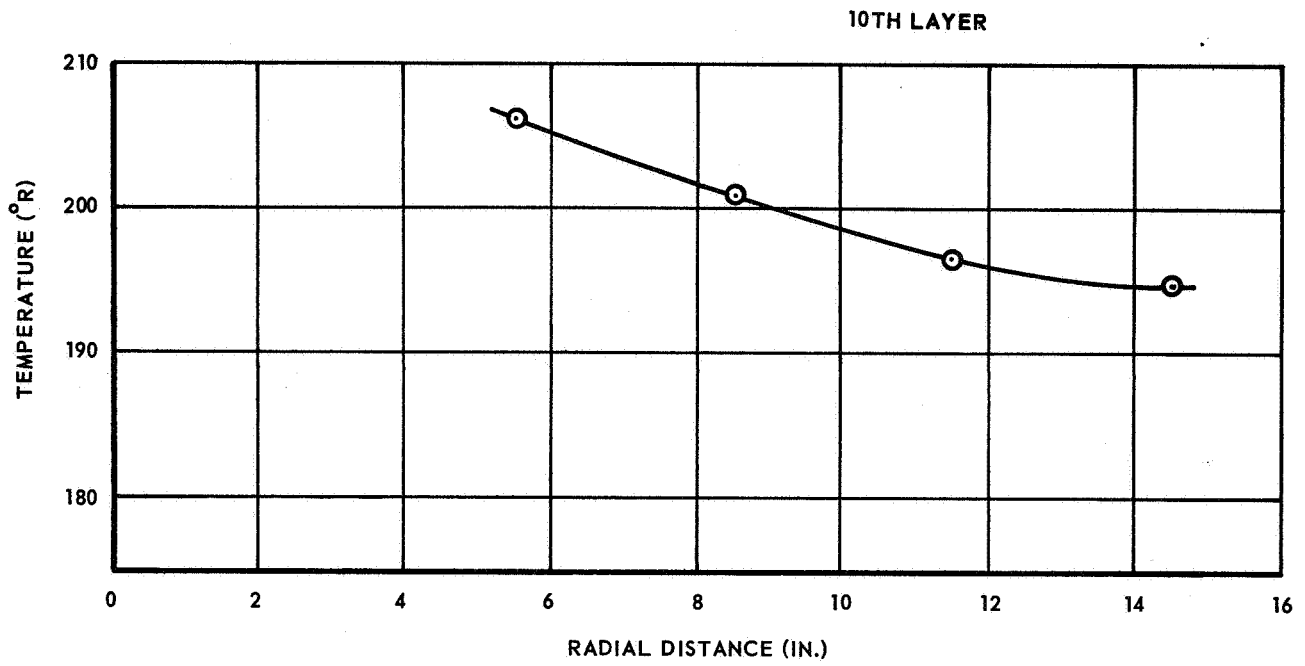


Fig. 11 Insulation Radial Temperature Distribution, Test 3

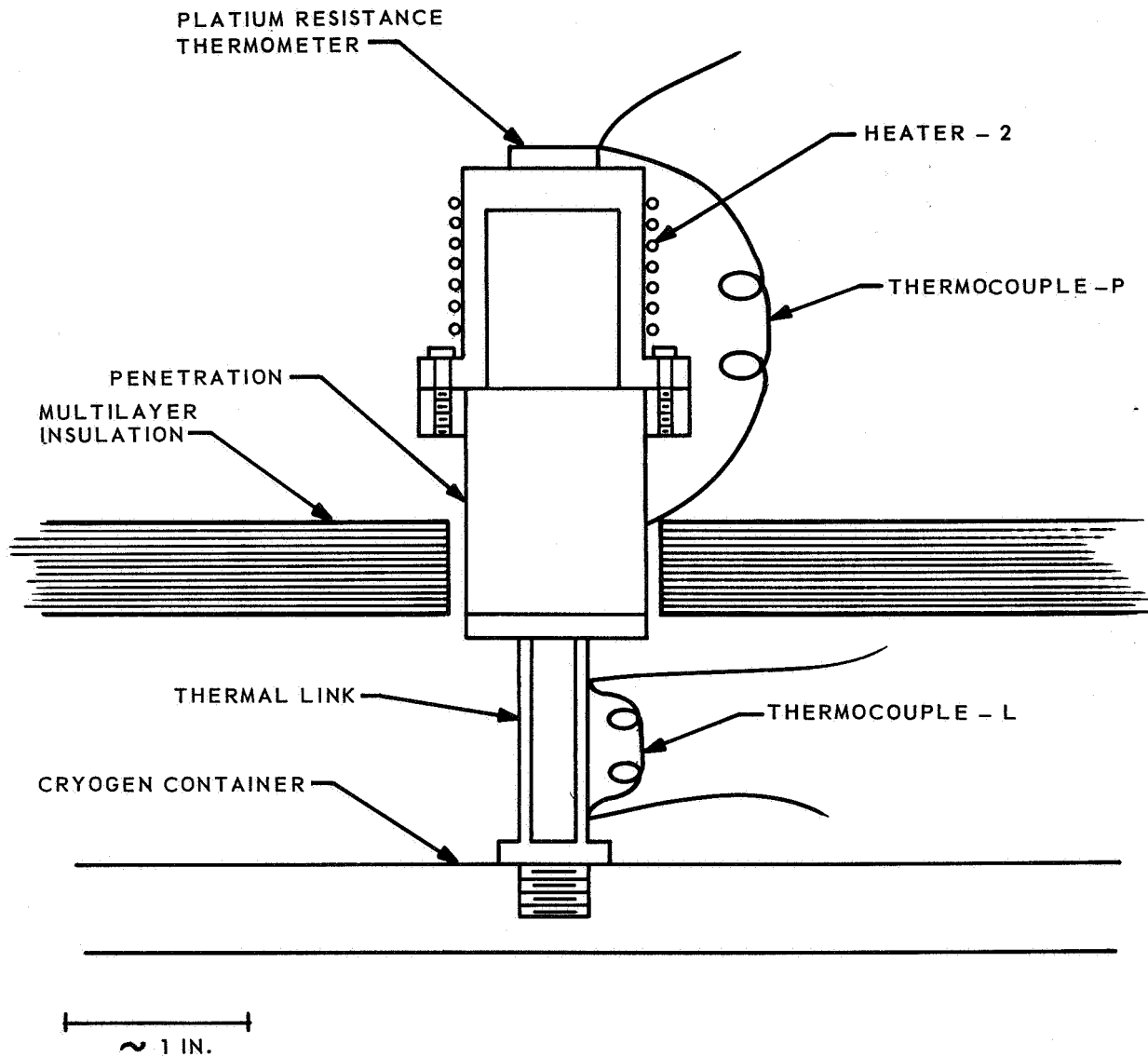


Fig. 12 Penetration Assembly

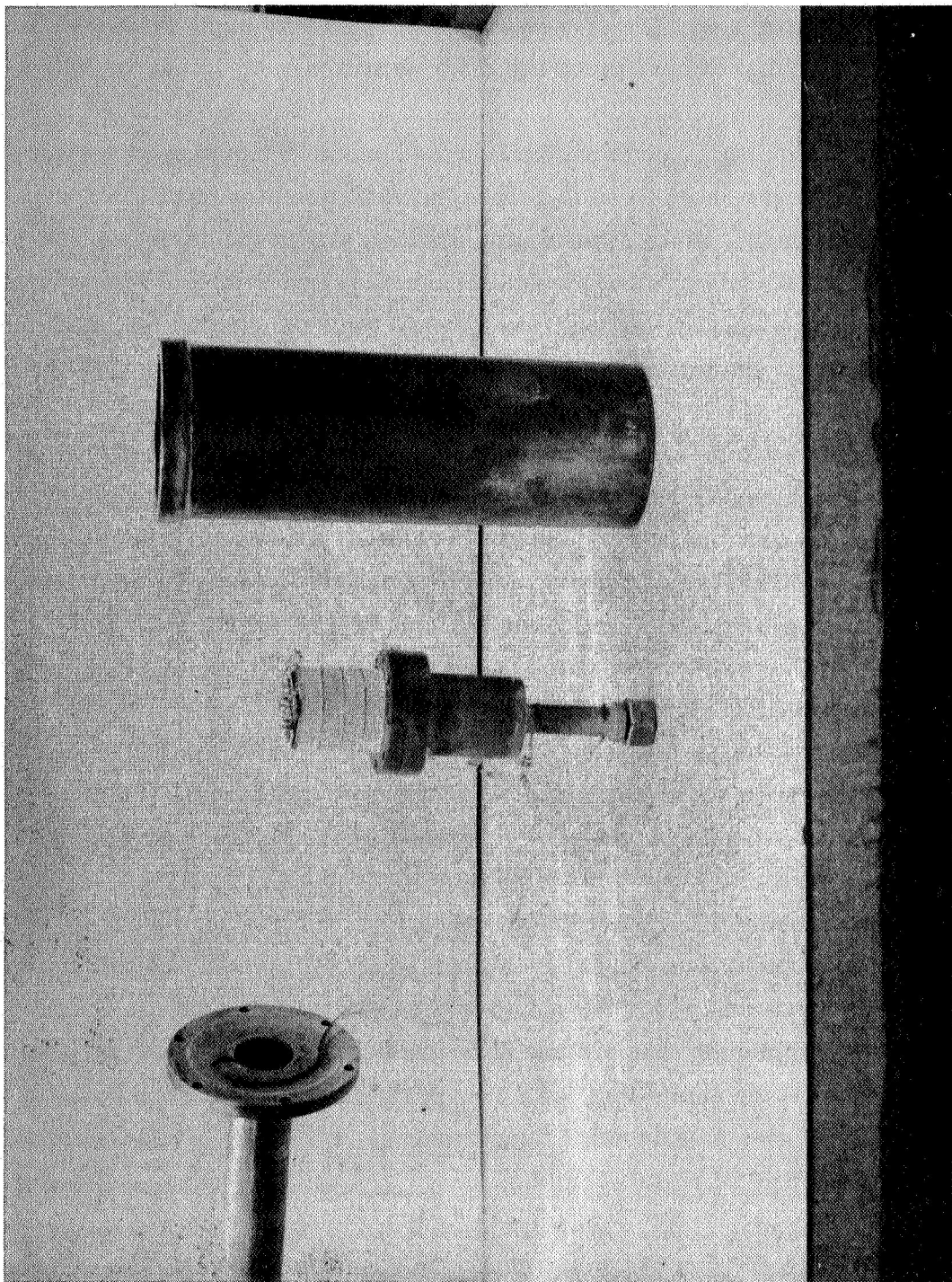


Fig. 13 Penetration and Calibration Apparatus

The penetration heater consists of a 300-ohm Evanohm wire heater wound and taped on the outside of a copper can. The copper can is fastened with eight screws to the copper ring which establishes heat contact to the penetration.

In the actual experimental configuration, multilayer insulation (not shown in Figure 12) is laid over the heater assembly so as to reduce the radiation heat input from the external warm surroundings. Disks of insulation are also placed inside the top and bottom areas of the penetration to reduce radiative heat transfer internal to the penetration. With these precautions the heat flow into and down the top section of the penetration is determined by the power input to the heater.

The thermal link, silver soldered to the bottom of the penetration, is machined from brass bar stock with the 1/4-in. I.D. by 3/8-in. O.D. section designed to produce a temperature drop of approximately  $6^{\circ}\text{R}$  over its 1-1/4-in. extension for a calculated heat load of 0.2 watt. This temperature gradient is measured with a gold-cobalt (Au-Co) differential thermocouple (T.C.-L) and gives the heat flow out of the bottom of the penetration provided that the conductivity of the brass is known.

Since the conductivity of brass will vary with composition, a calibration experiment was prepared to determine the temperature relationship of heat flow via the thermal link. The penetration assembly is thermally anchored to the bottom of an isothermal vacuum can (see Figure 11) by means of the same threaded link arrangement as used in the penetration cryostat. The lead wires to the platinum resistance thermometer, heater, and thermocouples are brought out through the 3/4-in. radiation-baffled pumping tube. A known amount of power is applied to the heater and, as the radiation heat transfer is quite small for the temperature differences involved, the thermal link is calibrated directly. At the same time, an Au-Co thermocouple is calibrated between the cryogen and resistance thermometer temperatures. This establishes the thermal emf curve for the T.C.-P of Figure 11.

Due to a change in vacuum chamber scheduling, this calibration experiment was abandoned in order to install the penetration cryostat for Tests 4 and 5. The calibration will be completed at a later date.

Tests 4 and 5

Tests 4 and 5 are with  $\text{LH}_2$  and  $\text{LN}_2$  cold boundaries with the penetration assembly installed and no intermediary insulation between the 1-in. O.D. stainless steel penetration and the multilayer insulation.

The data for these tests have not been completely analyzed to date. The radial and normal temperature distribution data for the  $\text{LN}_2$  RUN FOR NO HEATER power are presented in Figures 9 and 10; whereas previous temperature distributions had shown heat flow in a direction radially outward from the center with no penetration, and how the heat flow is reversed as expected to the direction of the penetration. The temperature of the colder 10th layer undergoes a larger perturbation under the influence of the penetration than the 40th layer.

For heater powers of .15 watt the temperature distributions are essentially unchanged (only  $1.5^\circ\text{R}$  in the colder layers). As this run preceded the calibration experiment, the heat flows were calculated on the basis of conductivities standard thermocouple tables, etc.

The data for no-power into the penetration heater, Case 1, showed the unexpected high heat load through the thermal link of 0.43 watt with a  $100^\circ\text{R}/\text{in.}$  gradient persisting across the penetration in the MLI area. The increase in heat flux,  $\Delta Q_c$ , to the cryogen (over Test 2) was  $.44 \pm .02$  watt, which is, within experimental error, equal to the thermal link heat flux,  $Q_L$ . If this were the case, there would be no change in the heat flux through the insulation, as

$$\Delta Q_c = Q_L + Q_{\text{ins}} \quad (1)$$

That this is not the case is evidenced by the radial temperature data and by the data for Case 2 with heater power,  $Q_H = .145$  watt. For this heater input the penetration temperature gradient increased to  $133^\circ\text{R}/\text{in.}$ ,  $Q_L$  to 0.48 watt, and  $Q_{\text{ins}}$  to  $+.17$  watt which is not consistent with Case 1.

Originally, a heat balance for the penetration was to be taken as

$$Q_L = Q_P + Q_X, \quad (2)$$

where  $Q_X$  is the heat transfer rate between the insulation and penetration, and  $Q_P$  is the heat flowing into the top of the penetration at the level of the top layer of insulation. In practice  $Q_P$  will be the sum of the heater power, and  $Q_H$  and  $Q_{RAD}$  will be the room temperature radiation heat input to the exposed top areas of the penetration heater. Equation 2 may then be written as

$$Q_L = Q_H + Q_{RAD} + Q_X \quad (3)$$

$Q_{RAD}$  was to have been kept small so that Eq. 2 would reduce to

$$Q_L = Q_H + Q_X \quad (4)$$

or

$$Q_X = Q_L - Q_H$$

However, with the large gradient across the penetration, it is doubtful that  $Q_{RAD}$  is unimportant. It is anticipated that further data reduction and analysis will resolve the discrepancy.

**TASK 2B: PARALLEL CONDUCTIVITY OF MULTILAYER INSULATIONS**

The final data for the double-aluminized Mylar-Dexiglas insulation test specimen were obtained during this reporting period. Additionally, a test specimen of NRC-2 insulation was fabricated and installed in the parallel conductivity cryostat. Data were obtained for this specimen with boundary temperatures at 252°R and 540°R.

An insulation specimen length of 3.4 inches was utilized for the final tests on the double-aluminized Mylar-Dexiglas. Previous data were obtained for specimen lengths of 11.0 and 7.4 inches. A summary of all data obtained for this initial insulation material is presented in Table 2 and shown graphically in Figure 14.

The main objective of obtaining data for variable lengths is to determine if radiation tunneling between the insulation layers is significant. From Table 2, it is seen that Test 13 data falls slightly below the previous data for a similar temperature range. The data for the 7.4-inch length (Test 12) should be compared with Tests 1 and 2 for an 11.0-inch sample length, while the data for the 3.4-inch sample length (Test 13) should be compared with Tests 2 or 3 for the 11.0-inch sample length, since similar hot and cold boundary temperatures were used in the corresponding cases. The slight deviation of this latest point is a result of experimental uncertainty (such as sample length) since reduction of sample length would result in a larger measured thermal conductivity if radiation tunneling were significant. From these tests the conclusion is reached that radiation tunneling is not significant for the double-aluminized Mylar-Dexiglas multilayer system for this layer density (approximately 82 layers per inch). It is probable that for other insulation systems or for a lower layer density radiation tunnelling is significant.

A sample of the NRC insulation was fabricated and installed in the parallel conductivity cryostat. The annular sample is 11 inches long (nominal) with a 4.5-inch inner diameter and a 1/2-inch thickness (nominal). The sample consists of 26 layers of the crinkled single-aluminized Mylar, i. e., layer density of approximately 50 layers/inch. The inner and outer guards have ten and eleven layers, respectively, and each guard is separated from the sample by two layers of 2.8-mil Dexiglas.

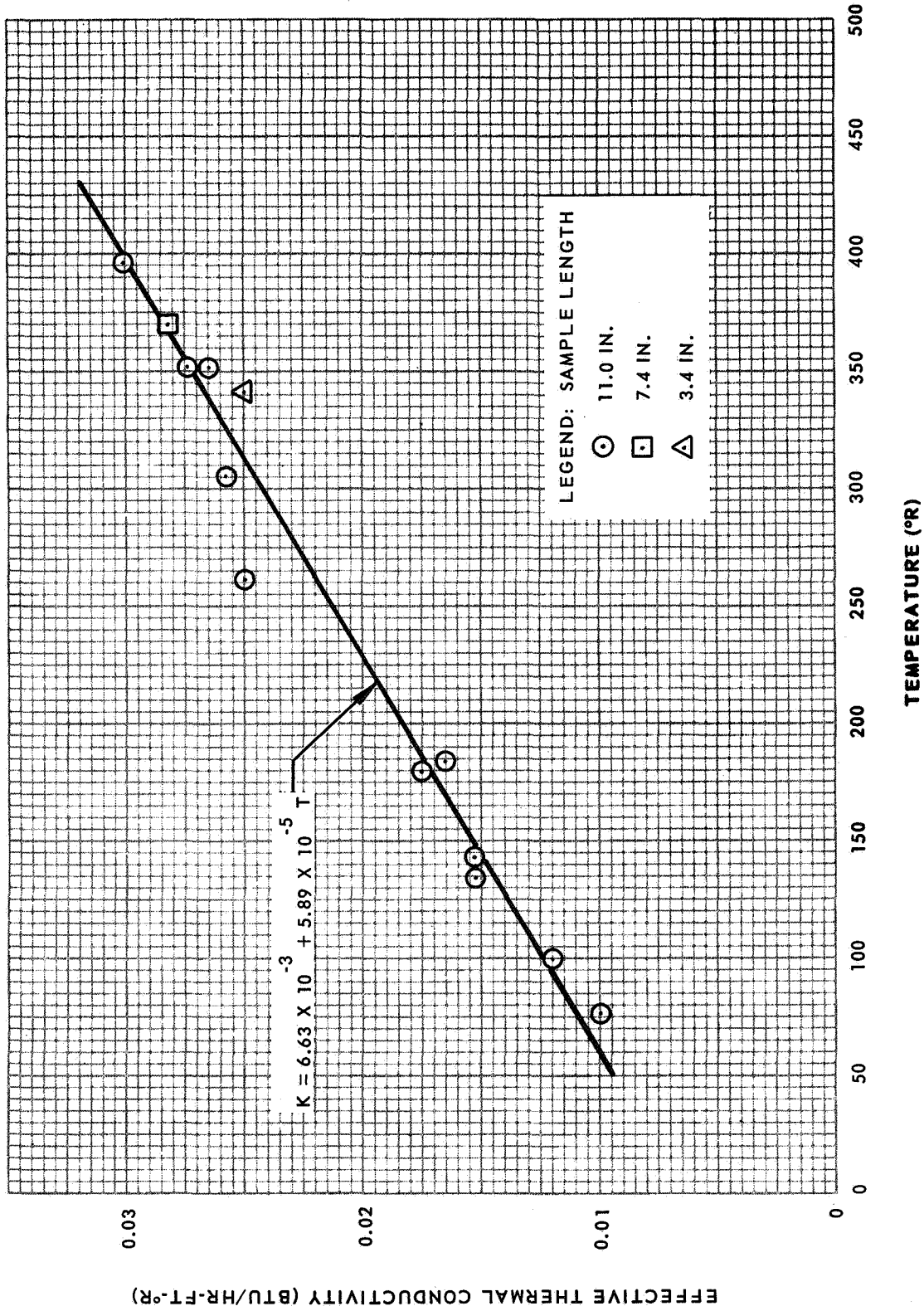


Fig. 14 Effective Thermal Conductivity of a Double-Aluminized Mylar - Dexiglas Multilayer Insulation System Measured Parallel to the Layers

Table 2

**EFFECTIVE THERMAL CONDUCTIVITY OF A DOUBLE-ALUMINIZED  
MYLAR-DEXIGLAS MULTILAYER INSULATION SYSTEM  
MEASURED PARALLEL TO THE LAYERS**

Test	Boundary Temp. (°R)	Sample Length (in.)	Cold Sink Fluid	Measurement Net Heat Flow (Btu/hr)	Effective Thermal Conductivity (Btu/hr-ft °R)
1	542-252	11.0	LN <sub>2</sub>	0.52	0.0301
2	451-252	11.0	LN <sub>2</sub>	0.31	0.0265
3	451-252	11.0	LH <sub>2</sub>	0.32	0.0273
4	359-252	11.0	LN <sub>2</sub>	0.162	0.0257
5	271-252	11.0	LN <sub>2</sub>	0.027	0.0251
6	206-162	11.0	LH <sub>2</sub>	0.043	0.0165
7	162-108	11.0	LH <sub>2</sub>	0.050	0.0154
8	253-108	11.0	LH <sub>2</sub>	0.151	0.0175
9	133-68	11.0	LH <sub>2</sub>	0.046	0.0120
10	216-69	11.0	LH <sub>2</sub>	0.134	0.0153
11	85.5-68	11.0	LH <sub>2</sub>	0.010	0.010
12	491-250	7.4	LN <sub>2</sub>	0.596	0.0282
13	434-250	3.4	LN <sub>2</sub>	0.88	0.025

Testing was begun on the sample using  $\text{LN}_2$  as the cold boundary heat sink. After obtaining the first calibration point at  $252^\circ\text{R}$ , a short in the bottom (hot boundary) heater developed. On removing the sample for repair, the silver epoxy potting at the cold boundary was also found to have broken away from the heater plates. The bottom heater and the potting of the cold boundary have been repaired and testing has resumed using  $\text{LN}_2$  as the cold boundary heat sink. The calibration point has been rerun at  $252^\circ\text{R}$ , and the first test point with  $252^\circ\text{R}$  cold and  $540^\circ\text{R}$  hot boundary temperature has been obtained. The net heat flow through the sample was 0.554 Btu/hr, which corresponds to an effective sample parallel conductivity of 0.0324 Btu/hr-ft  $^\circ\text{R}$ . This can be compared to Test 1 of Table 2, for which the measured conductivity was 0.0301 Btu/hr-ft  $^\circ\text{R}$ . Based solely on the "bulk" thermal conductivity of the aluminum film on the single-aluminized Mylar of estimated 400Å aluminum film thickness, the effective thermal conductivity should be approximately 0.013 Btu/hr-ft  $^\circ\text{R}$  at  $396^\circ\text{R}$  mean temperature. The considerably higher measured conductivity than predicted solely from aluminum conduction suggests that radiation tunnelling in the NRC insulation represents a significant if not predominate mode of energy transfer for the temperature range of this test. This is not too surprising since the layer density of the sample being tested (which provides a minimum perpendicular thermal conductivity) is quite loose, thus allowing many reflections, whereas the previous specimen had almost twice the number of radiation shields, as well as the Dexiglas spacer material which will scatter thermal radiation.

Additional tests will be made with the nominal 11-inch sample including two tests, ( $252$ - $360^\circ\text{R}$  and  $162$ - $216^\circ\text{R}$ ) with  $\text{LN}_2$  as the cold sink, and a single test ( $72$ - $154^\circ\text{R}$ , approx.) with  $\text{LH}_2$  as the cold sink. The sample will then be reduced to a nominal 4-inch length, and two tests will be run with  $\text{LN}_2$  as the cold sink to determine the significance of radiation tunnelling.

#### Data Analysis

When thermal conductivity is a function of temperature and data is obtained for large differences between hot and cold boundary temperatures as is the case in the current measurements, the question arises as to what is the effective temperature at which

the data should be plotted. In presenting the data in the past, the data point is plotted at the mean of the hot and cold boundary temperature, and the temperature range for each measurement is indicated by arrows. In general, the effective temperature is not necessarily the mean temperature.

Assuming a functional relationship for  $k = f(T)$ , then the effective temperature for a measurement made over specified end temperatures can be computed. The present data indicate that a linear relation  $k = a + bT$  appears to be a good approximation in general over the entire range. Therefore, considering a smaller interval corresponding to an individual test the linear approximation is even better. Making the linear approximation then for steady state

$$\frac{d}{dx} \left[ (a + bT) \frac{dt}{dx} \right] = 0$$

Integrating twice:

$$aT + \frac{1}{2}bT^2 = Ax + B$$

Inserting the limits:

$$\text{At } x = 0, T = T_H \text{ and at } x = L, T = T_C$$

$$B = \left( a + \frac{b}{2} T_H \right) T_H$$

$$C = \frac{1}{L} \left[ \left( a + \frac{b}{2} T_C \right) T_C - \left( a + \frac{b}{2} T_H \right) T_H \right]$$

Therefore:

$$T^2 + \frac{2a}{b} T - \frac{x}{L} \left[ \left( \frac{2a}{b} + T_C \right) T_C - \left( \frac{2a}{b} + T_H \right) T_H \right] - \left( \frac{2a}{b} + T_H \right) T_H = 0$$

and on solving for T:

$$T = \left\{ \frac{x}{L} \left[ \left( \frac{2a}{b} + T_c \right) T_c - \left( \frac{2a}{b} + T_H \right) T_H \right] + \left( \frac{a}{b} + T_H \right) 2 \right\}^{\frac{1}{2}} - \frac{a}{b}$$

The location  $(x/L)_e$  within the sample where the gradient  $-\frac{dT}{dx}$  equals  $(T_H - T_c)/L$  is determined by equating the latter to the derivative of the above equation:

$$\left( \frac{x}{L} \right)_e = \frac{\frac{a}{b} + \frac{1}{4} (T_c + 3 T_H)}{\frac{2a}{b} + (T_c + T_H)}$$

and the temperature  $T_e$  at  $(x/L)_e$  is

$$T_e = \frac{1}{2} (T_c + T_H)$$

Therefore, for a linear variation of  $k$  with  $T$  the temperature which corresponds to the computed thermal conductivity is the mean temperature. This is simply a property of the parabolic temperature distribution resulting from a linear thermal conductivity variation.

The experimental data points plotted at the mean sample temperature therefore can be quite adequately expressed in terms of a linear function as determined from a least-squares curve fit

$$k = 6.63 \times 10^{-5} + 5.89 \times 10^{-5} T$$

where the dimensions of  $k$  and  $T$  are Btu/ft-hr  $^{\circ}R$  and  $^{\circ}R$ , respectively. In actuality a curve which has an asymptotic behavior at higher temperature as illustrated by the dashed line is probably more realistic since the conductivity of aluminum is fairly constant at higher temperature; however, the linear expression above is adequate only for the temperature range covered.

### Temperature Dependence of Parallel Thermal Conductivity in Multilayer Insulation

In the multilayer insulation systems investigated to date, the three mechanisms of thermal energy transfer (solid conduction, radiation tunneling, and gas conduction or convection) could all occur. For the pressures at which these multilayer insulations are used and at which the experiments were conducted ( $\approx 10^{-5}$  mm Hg) heat transport through the gas is negligible. Furthermore, from the measurements made with variable sample length the radiation "tunnelling" between layers was inferred to be insignificant (other insulation systems may exhibit a significant tunnelling effect). Solid conduction can occur in all three materials comprising the insulation: aluminum film, Mylar, and Dexiglas spacer. The approximate thicknesses per layer of insulation are between 755 and 1050 Angstroms for the aluminum (sum of both films), 0.25 mil for the Mylar, and 2.8 mils for the Dexiglas. The thermal conductivities at room temperature are approximately 130, 0.09, and 0.0006 Btu/hr-ft<sup>2</sup>°R for the aluminum, Mylar, and Dexiglas, respectively. From these values it is seen that the conduction through the aluminum films is at least 20 times that through either the Mylar or Dexiglas; therefore, it would be reasonable to consider only the aluminum contribution to heat transfer as a first approximation.

Both electrons and phonons (lattice vibrations) contribute to heat transport in solids. However, in relatively pure metals, such as the aluminum film on the Mylar, the contribution due to phonons is of little importance since there is a large supply of free electrons, i.e., relatively pure metals exhibit high electrical conductivity. On the other hand, for impure metals, alloys, and semiconductors, where there are few "free" electrons, a substantial proportion of the thermal conduction is due to lattice conduction; and in dielectric crystals all thermal energy is transported by phonons. The following discussion is limited to electronic heat conduction.

From kinetic theory, the thermal conductivity can be expressed as:

$$k = Aclv$$

where  $A$ ,  $c$ ,  $l$ , and  $v$  are, respectively, a constant (usually  $1/3$ ), the specific heat of the carrier per unit volume, the mean free path of the carrier (average distance between collisions), and the velocity of the carriers. For electrons the velocity is constant and the electron specific heat varies linearly with temperature (up to  $30,000^{\circ}\text{K}$ ). The thermal conductivity therefore varies as:

$$k \propto Tl$$

Resistance to electron motion may occur due to (1) scattering due to various distortions, such as actual impurities, lattice defects and boundaries, etc., and (2) scattering of electrons due to thermal vibrations of the atoms; this latter effect occurs in even absolutely pure metals. The effective mean free path " $l$ " results from a combination of both effects. At room temperature for aluminum the mean free path is approximately 500 to 1000 Angstroms (Ref. 1), and since the bulk aluminum exhibits an increase in conductivity with decreasing temperature (until a maximum is reached near  $50^{\circ}\text{R}$ ) the mean free path must increase even faster than  $1/T$  because of the above relation. However, the aluminum film thickness is of the order of 400 Angstroms on each side of the Mylar. The thermal conductivity of the film will, therefore, be governed by the film thickness which is smaller over the entire range tested. The mean free path is, therefore, invariant with temperature, and the thermal conductivity should exhibit a linear temperature variation as is approximately the case for the measured experimental data. Other effects, such as the possible contribution of the Mylar, would be expected to show an increasing contribution at lower temperatures; however, this cannot be inferred from the experimental data. It is interesting that the aluminum film thickness and room temperature electronic mean free path in bulk aluminum by chance are of the same magnitude, resulting in a linear conductivity over the entire temperature range. Had the film thickness been several times larger, the conductivity would exhibit a slight increase with decreasing temperature below room temperature; then a peak at somewhat higher temperature than bulk aluminum maximum would be followed by a steep reduction at lower temperatures.

## PHASE II. THERMAL DESIGN HANDBOOKS

### TASK 1: OPTICAL PROPERTIES HANDBOOK

In this reporting period work was initiated in this area to further define and organize the efforts to be expended. A decision was made to incorporate in the handbook only presently available data and information. The basic format to be utilized is that of the Thermophysics Design Handbook, LMSC 8-55-63-3. In some cases of the new handbook data updating is required, while complete revisions are needed in other sections. Following is a brief outline of the revisions and additions to the Thermophysics Design Handbook.

#### Section 4: Thermal Design Techniques

4.1 Thermal Control Surfaces. In this section the solar reflector coating will be divided into the solar reflector diffuse class of coatings (i.e., white paints) and the solar reflector specular coatings (i.e., solar concentrator and mirror coatings).

#### Section 6: Effects of the Spacecraft Environment on Thermal Control Materials

6.2 Prelaunch Environmental Effects. Add presently used methods of protecting thermal control materials.

6.4.1 Planetary Atmospheres-Vacuum. The discussion on sputtering will be rewritten to reflect actual flight experimental data demonstrating no problem except possibly for highly elliptical orbits.

6.4.2 Solar Electromagnetic Radiation. This section will be rewritten to reflect our increased knowledge of the fundamental damage mechanisms in some white coatings.

6.4.3 Penetrating Radiation. This section will be rewritten to reflect our present knowledge of the particle electromagnetic environment of space, and we will report on the importance of combined environmental simulation. The important regions of space to be aware of as far as charged particle damage will be documented so that the spacecraft thermal designer is aware of potential problem areas.

6.4.4 Meteoroids. The references to the meteoroid environment will be updated and the relative importance of this environment will be documented.

6.4.5 Temperature. As this handbook will be directed in general towards the cryogenic stage designer, this section will be greatly expanded to include the effects of cryogenic temperature substrates on thermal control coatings, such as paints and metallized coatings.

## Section 8

In this section our intent is to add thermal design data on new production materials in use at LMSC since the original handbook was written (i.e., LMSC Thermatrol, LMSC Optical Solar Reflector, Grey Thermatrol, and Kemacryl). The tolerance to the space environments, as measured "in situ" will be presented for the Thermatrol coating. Additional properties data such as specific heat, thermal conductivity, density, and minimum thickness for opacity will be added for those coatings when available.

A section will be added on promising research coatings, their present status, and known properties. These coatings include the NASA-Ames/LMSC electron beam deposited coatings and the LMSC Lockspray gold coatings.

A rough draft write-up has been prepared on Lockheed Research Coating Systems. The coatings which were concentrated on were low absorptance, variable emittance, and optical thin films which have been prepared by physical vapor deposition. Data on the effect of dielectric emitter layer thickness on the solar absorptance and total hemispherical emittance of gold, silver, and aluminum overcoated with silica or alumina dielectric is given. The write-up also includes a discussion of the importance of

deposition parameters, advantages and disadvantages of this class of thermal control surface, and the environmental stability of the coatings.

This text, when completed, will be included in a new materials section of the handbook which has the tentative title, "Research Coatings".

Past data on the LMSC Thermatrol air-drying, white, thermal control coating has been compiled, and efforts to put the data into a formal form are in progress. This data includes the degradation characteristics of the coating when exposed to simulated ultraviolet radiation with the damage being measured "in situ". Data on exposure rates of 20 suns, 15 suns, and 1 sun are given to document that reciprocity relationships do not hold true for simulated solar ultraviolet testing on ZnO and TiO<sub>2</sub> pigmented coatings.

A write-up documenting the important constituents of the space environment to be concerned with in defining spacecraft surface optical damage is approximately 60 percent completed. The specific environments which are receiving attention include auroral electrons and protons, the artificial electron belt, natural low-energy, geomagnetically trapped electrons and protons, and solar-wind protons. The solar ultraviolet environment of space is also included. Minor environments which are briefly mentioned include residual atmospheric particles, solar flare protons, solar x-rays, and micro meteoroids.

A write-up on the "state-of-the-art" methods used in obtaining thermal design data has been initiated. Important additions to the present handbook discussion include the "in situ" laboratory apparatus for ultraviolet degradation determinations, combined elementary charged-particle/ultraviolet exposure chambers with "in situ" instrumentation, and advanced surface stability flight experiments which include integrating spheres and the capability to segregate charged particle effects, electromagnetic effects, and combined charged particle-plus-electromagnetic environmental effects.

A write-up on a section to the handbook which describes the effects of cryogenic temperatures ( $\approx 77^{\circ}\text{K}$ ) on the ultraviolet stability and physical properties of selected low  $\alpha_s/\epsilon$  thermal control coatings is approximately 20 percent complete. Liquid nitrogen bend, flexibility, abrasion, adhesion, and temperature cycling tests were used for the evaluation of physical properties.

## PHASE III. GAS FLOW STUDIES

### TASK 1: OUTGASSING STUDIES

During this reporting period the bulk of the testing has been completed. Table 3 lists and describes the tests completed to date. In the early stages of testing, the data acquisition technique employed was the pressure-rise method originally proposed. With this technique an insulation specimen is placed in a vacuum chamber and evacuated for some predetermined length of time. The vacuum chamber is then isolated from the vacuum pumps, and the chamber pressure rise as a function of time is recorded. Ostensibly, by performing this test on a vacuum chamber, both with and without an insulation specimen present and noting the difference in pressure rise, the insulation outgassing rate can be determined. However, as testing progressed, it was found that in some cases there was no perceptible outgassing from certain specimens, while with others in the chamber the pressure rise was lower than with the empty chamber. It was, therefore, concluded that the insulation specimens were actually sorbing chamber outgassing, thus precluding the possibility of obtaining useful data from this experimental approach. As a result, the pressure-rise technique was abandoned in favor of a new approach in which the outgassing rate is determined from comparison of the vacuum chamber pump-down characteristics when empty and with an insulation specimen present.

#### Experimental Data

The results of the tests listed in Table 3 are presented in graphical form.

Figures 15 and 16 show the effect of pumping time before close-off for the empty chamber using initial environments of dry air and 100 percent humid air, respectively. They show a scatter of data of about  $\pm 3$  percent for the humid air. It is apparent that pump-down times slightly greater than seven minutes would be necessary to achieve a pump-down-time-independent pressure rise rate. From these data it was decided that a

Table 3

SCHEDULE OF COMPLETED TEST RUNS

Test No.	Sample Type	No. of Min. Exposed to One Atmosphere Environment	No. of Min. Pumped Before Test Chamber Was Closed Off	Type of Gaseous Environment	Comments
1	None	0.2	1	Dry Air	19 Shts. 6 in. x 6 in.
2	↓	↓	1	100% Humid Air	
3	↓	↓	3	↓	
4	↓	↓	5	↓	
5	NRC Single-Aluminized Mylar	10	1	Dry Air	
6	↓	5	3	↓	
7	↓	5	(Pump Down)	↓	
8	↓	5	3	↓	
9	↓	↓	5	↓	
10	↓	↓	7	↓	
11	Dexiglass	↓	1	↓	19 Shts. 6 in. x 6 in.
12	↓	↓	3	↓	
13	↓	↓	5	↓	
14	↓	↓	7	↓	
15	↓	↓	(Pump Down)	↓	
16	↓	↓	1	100% Humid Air	200 Shts. 6 in. x 6 in.
17	None	↓	1	Dry Air	
18	↓	↓	3	↓	
19	↓	↓	5	↓	
20	↓	↓	7	↓	
21	NRC	(Pump Down in Off-Shelf Condition.)			
22	↓	5	5	Dry Air	
23	NRC	5	(Pump Down)	Dry Air	

Table 3 (Cont.)

Test No.	Sample Type	No. of Min. Exposed to One Atmosphere Environment	No. of Min. Pumped Before Test Chamber Was Closed Off	Type of Gaseous Environment	Comments		
24	NRC	5	5	Helium	Specimen at Liquid Nitrogen Temp. Specimen was Inadvertently Heated to 300°F Heated to 300°F Specimen at Liquid Nitrogen Temp. 200 Shts. 6 in. x 6 in. Offshelf Specimen at LN <sub>2</sub> Temp. Specimen at LN <sub>2</sub> Temp. 200 Shts. 6 in. x 6 in.		
25	↓		↓	↓			
26	↓		↓	↓			
27	↓		↓	↓			
28	↓		↓	↓			
29	↓		↓	( Pump Down)			
30	None		↓	5			
31	↓		↓	( Pump Down)			
32	↓		↓	5			
33	↓		↓	( Pump Down)			
34	↓		↓	5			
35	↓		↓	( Pump Down)			
36	↓		↓	5			
37	Aluminum Foil 1 Dexiglas		↓	( Pump Down)			
38	↓		↓	5			
39	↓		↓	( Pump Down)			
40	↓		↓	5			
41	↓		↓	↓			
42	None		↓	↓			
43	↓		↓	↓			
44	None		↓	( Extended Pump Down)			
						Dry Air	↓

Table 3 (Cont.)

Test No.	Sample Type	No. of Min. Exposed to One Atmosphere Environment	No. of Min. Pumped Before Test Chamber Was Closed Off	Type of Gaseous Environment	Comments
45	NRC		(Extended Pump Down)	Off Shelf	Specimen at LN <sub>2</sub> Temp. 200 Shts. 6 in. x 6 in.
46	↓	5	↓	Dry Air	
47	↓	5	↓	↓	
48	Dexiglas		↓	Off Shelf	
49	↓	5	↓	Dry Air	
50	↓	5	↓	↓	
51	Aluminum Foil		↓	Off Shelf	
52	↓	5	↓	Dry Air	
53	↓	5	↓	↓	
54	Double Aluminum Mylar		↓	Off Shelf	
55	↓	5	↓	Dry Air	
56	↓	5	↓	↓	

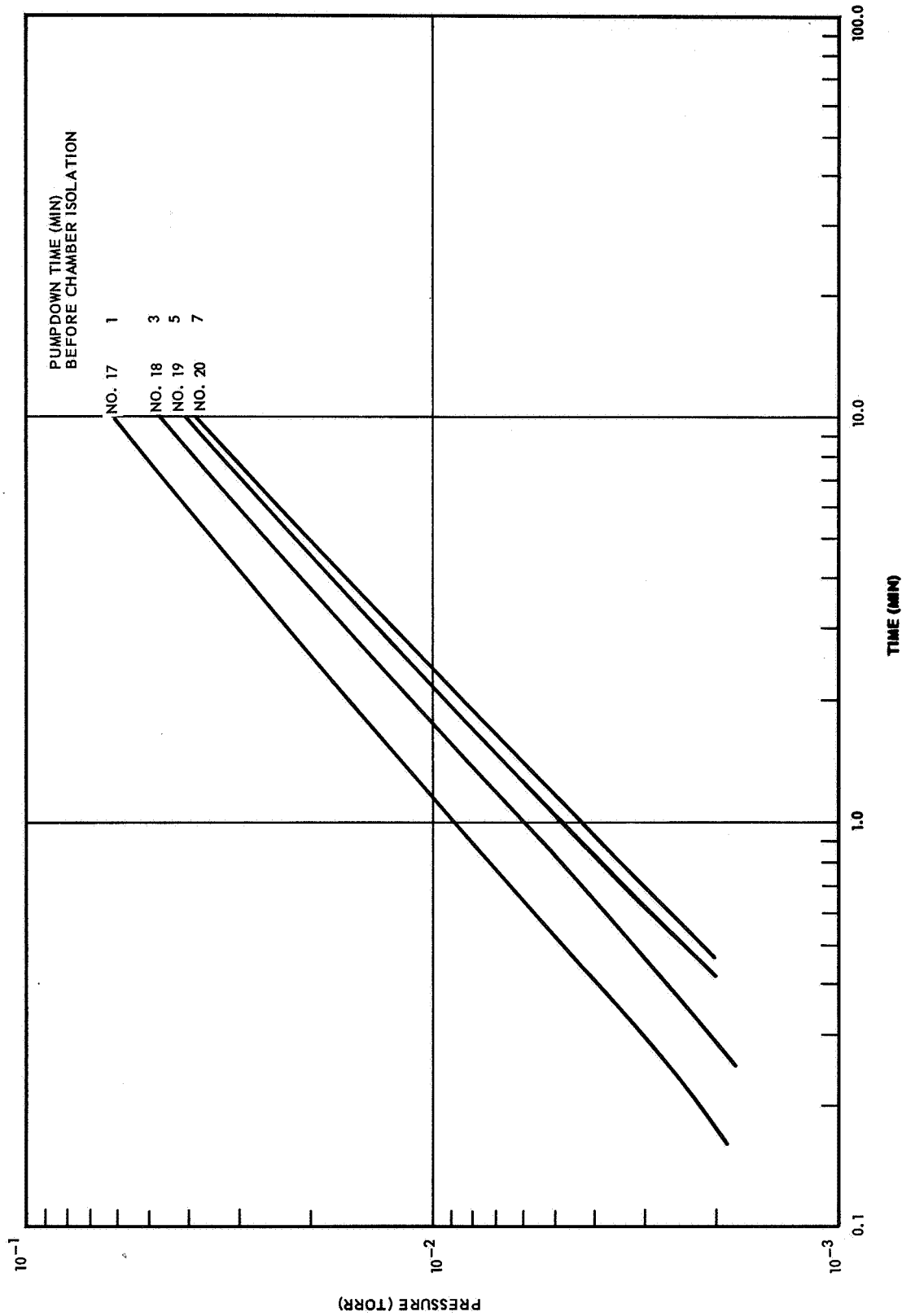


Fig. 15 Empty Vacuum Chamber Pressure - Rise Characteristics  
With Dry Air at Ambient Temperature

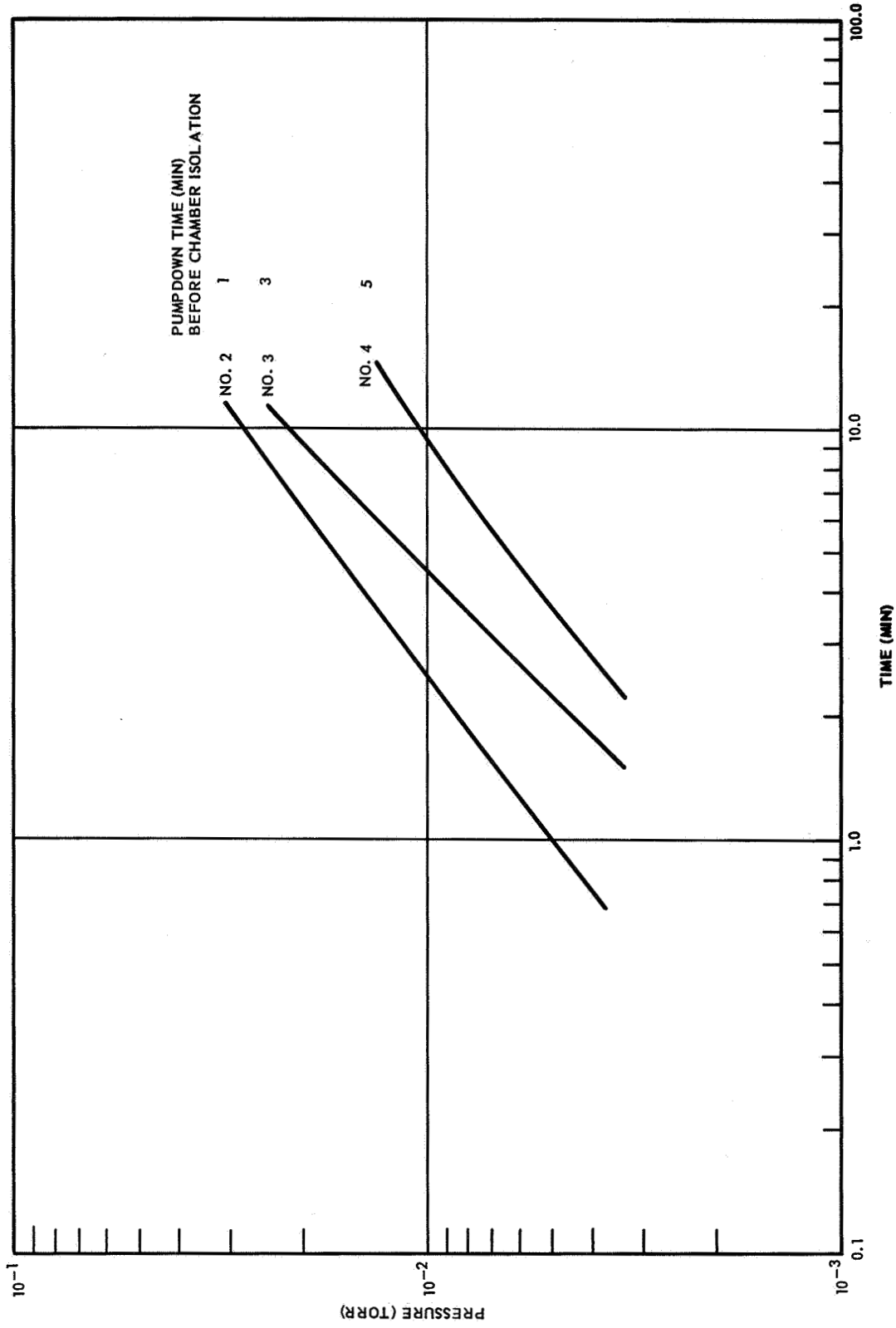


Fig. 16 Empty Vacuum Chamber Pressure - Rise Characteristics After Being Subjected to 100 Percent Humid Air at Ambient Temperature

compromise would be necessary in the choice of a standard pump-down time if excessive experimental durations were to be avoided. By arbitrary means, five minutes was chosen as the standard time for exposure to the one atmosphere environment. This was based on the observation made in preliminary runs that most of the sorption took place almost instantaneously and that insufficient time or knowledge was available to assess what might be gained by longer exposures than the seemingly reasonable time chosen.

Figure 17 shows pressure rise curves for the chamber with and without NRC crinkled single-aluminized Mylar insulation, Dexiglas, and aluminum foil and Dexiglas (Tests 13, 19, 22, 36, and 38). The NRC specimen was comprised of 200 sheets of 6 in. x 6 in. in a stack about 1-1/2 in. high. It can be seen that the curve for the NRC in the chamber essentially follows the empty-chamber curve within experimental accuracy. This suggests that the outgassing rate of the Mylar was too small relative to the chamber outgassing rate for the sensitive measurement to be made. Another possibility is that the NRC sample was very nearly at equilibrium concentration at the time and pressure of close-off. As the pressure rose due to chamber outgassing, the NRC sample may have taken up some of this gas, or, at least, stopped outgassing any further. In any case, it is appropriate to estimate the sensitivity of the apparatus for this type of experiment. The pressure rise characteristic for Test 19 on Figure 15 has the equation

$$P = 4.8 \times 10^{-3} t^{0.92} \text{ torr} \quad (5)$$

where  $t$  is in minutes. Differentiation of this relation gives

$$\begin{aligned} \frac{dP}{dt} &= 0.92 \times 4.8 \times 10^{-3} t^{-0.08} \text{ torr/min} \\ &= 2.74 \times 10^{-3} P^{-0.087} \text{ torr/min} \end{aligned} \quad (6)$$

The volumetric outgassing rate  $Q_o$  is given by

$$Q_o = \frac{V}{P} \frac{dP}{dt} \text{ cm}^3/\text{min} \quad (7)$$

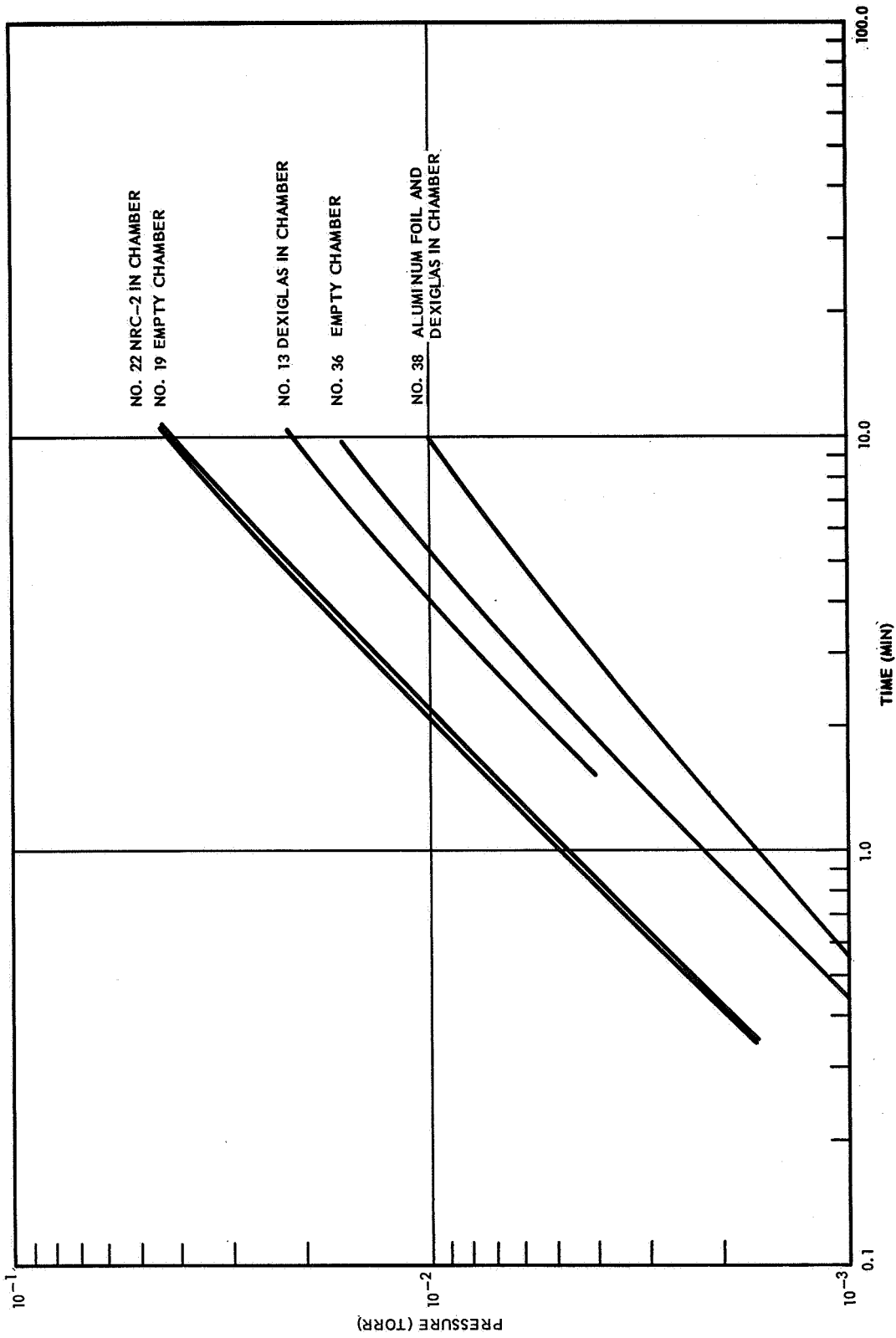


Fig. 17 Vacuum Chamber Pressure-Rise Characteristics With Various Insulation Specimens Present at Ambient Temperature After Being Exposed to Dry Air

The mass outgassing rate for this chamber of volume  $V = 38,670 \text{ cm}^3$  assigned to a sample area of  $93,000 \text{ cm}^2$  is thus

$$PQ_0 = \frac{38,670}{93,000} \times 2.74 \times 10^{-3} P^{-0.087} \text{ torr cm}^3/\text{cm}^2 \text{ min} \quad (8)$$

At  $P = 10^{-3}$  torr this amounts to  $0.000624 \text{ torr cm}^3/\text{cm}^2 \text{ min}$ . The small exponent of  $P$  in the last equation makes this quantity almost independent of pressure. It may be assumed that the minimum detectable sample outgassing would have to be at least 10 percent of this, or  $0.0000624 \text{ torr cm}^3/\text{cm}^2 \text{ min}$ . Data to be presented later in this report shows that the outgassing rate of NRC insulation after cycling with any air is of the order of  $0.01 \text{ torr cm}^3/\text{cm}^2 \text{ min}$  after five minutes of pumping, and that a substantial amount of outgassing occurs in this period. It is thus concluded that the apparatus sensitivity is not too low, but that the NRC sample is sorbing outgassed material from the chamber walls, rendering the experiment meaningless.

It was important in the above instance to show quantitatively that the chamber sensitivity was adequate for the experiment and that another explanation was necessary. The explanation given that the sample was acting as a "getter" for the chamber is more dramatically shown in the curve for Tests 13 and Tests 36 and 38. It is shown that the rate of pressure rise for the chamber with 19 sheets of 6 in. x 6 in. Dexiglas is less than that of the empty chamber. Tests 36 and 38 show the same anomaly for a sample of a total of 200 sheets, 6 in. x 6 in., of alternate layers of Dexiglas and aluminum foil. (The difference in the empty chamber characteristics, Tests 38 and 19, is due to a chamber modification between Tests 34 and 35.) These figures can only be explained as showing the "gettering" action of the Dexiglas; it is assumed that the contribution of the aluminum foil was small.

Fig. 18 shows the close-off curves for the NRC insulation sample exposed initially to an atmosphere of helium and held at ambient and liquid nitrogen temperatures. Two sets of lines are shown for each test. The lower set are plotted directly from the Alphasatron gauge reading, which is accurate for dry air. If helium pressure is being measured, then the scale reading must be multiplied by 4.76 for the pressure gauge correction, which is how the upper pair of lines were obtained from the lower pair.

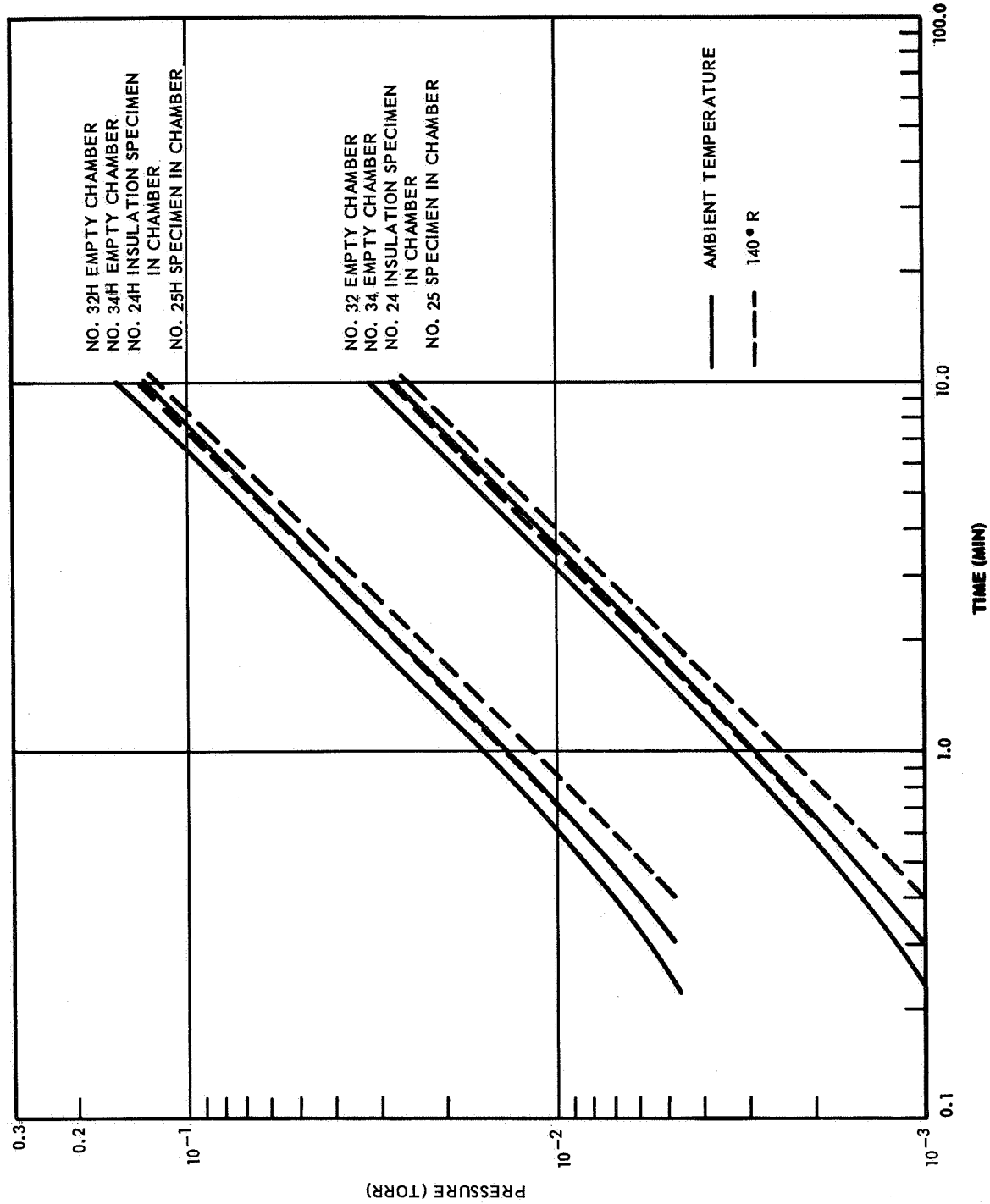


Fig. 18 Pressure-Rise Characteristics of Vacuum Chamber With and Without Specimen of Crinkled Mylar Aluminized on One Side (NRC-2) at Ambient Temperature and at 140°R

However, the upper set seems to indicate far too high pressures. It is suspected that this indicates that a substantial part of the gas being released by the chamber walls was not helium so that the true curves should lie somewhere between the two sets drawn, but exactly where they are can not be determined until the gas specimens are analyzed. Assuming that gas composition variations between tests are small, it may be concluded from Fig. 18 that little difference in outgassing rate is observed between ambient and liquid nitrogen temperature conditions. Also, the NRC sample is apparently "gettering" the gas evolved from the chamber walls in the same manner as the Dexiglas did in the previously mentioned tests. Since helium tends to adsorb in only a very slight degree, it seems likely that the surface of the NRC sample will be relatively "clean" in these tests and will be a better adsorber than in the dry air tests.

Figure 19 shows the close-off curves for the aluminum foil/Dexiglas sample for the case of helium at ambient and liquid nitrogen temperatures, respectively. The ambient temperature case again shows the "gettering" effect of the sample, but the low temperature case is anomalous in that the sample shows a positive contribution to the system outgassing rate. Of course, this is the type of result that was anticipated in the originally proposed experiments; however, since the "gettering" effect has been shown so clearly in other cases, it must certainly be present here also. The most plausible explanation for this behavior is that helium is soluble in borosilicate glass of which Dexiglas is composed. The diffusion process has a longer relaxation time than surface desorption; thus the departure of helium from Dexiglas will be at a relatively slow rate and will continue for a substantial period after close-off. Further, the flow path out from between the Dexiglas layers has a higher resistance than for the NRC specimen, so this too may hold up the outgassing of the sample during the five-minute pump-down.

Having concluded that no useful data could be obtained from the close-off experiments, pump-down experiments were conducted. These consisted simply of measuring pressure and time for the evacuation of the chamber both with and without the sample present. Only the mechanical pump was used for evacuation of the chamber. Initial tests showed that the presence of outgassing could be detected quite easily by this method. It was also shown that the outgassing from a sample straight from the roll, or in "off-shelf" condition, was likely to be very different from a sample repeatedly cycled under experimental conditions.

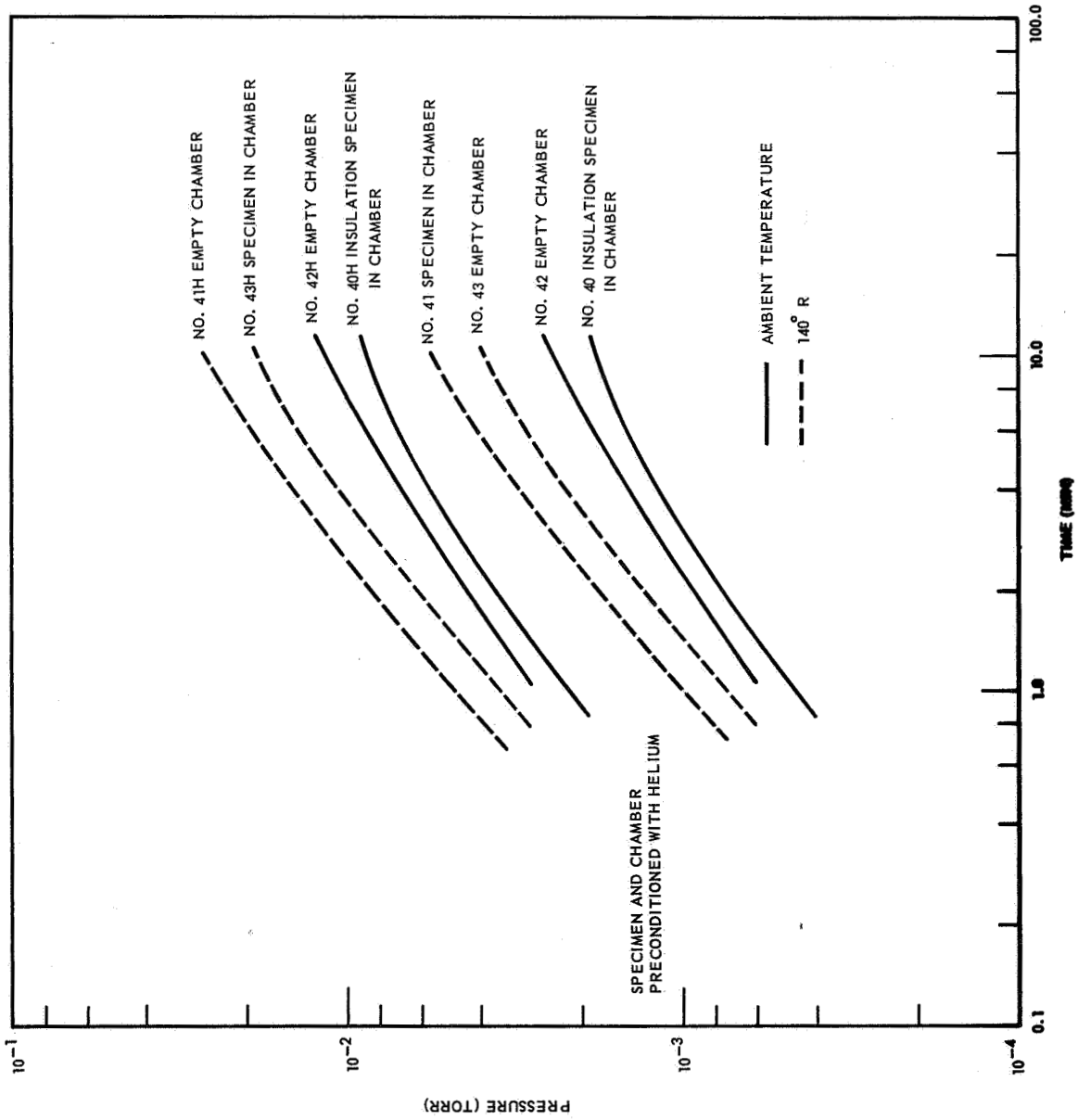


Fig. 19 Pressure-Rise Characteristics of Vacuum Chamber With and Without Specimen of Aluminum Foil and Dextraglas at Ambient Temperature and  $140^{\circ}R$

The preliminary tests were numbers 7, 15, 21, 23, 29, 31, 33, 35, 37, and 39. The data from them are not reported here since they were repeated and extended in tests to be discussed later in this report.

Outgassing rates may be determined from knowledge of pump-down curves as follows. From the measurements of pressure  $P$  and time  $t$  the slope of the curve  $\frac{dP}{dt}$  may be found. This term is related to the outgassing rate in the equation

$$Q_P = Q_o - \frac{V}{P} \left( \frac{dP}{dt} \right)_o \quad (9)$$

where  $Q_o$  is the empty chamber outgassing rate,  $Q_P$  the chamber pumping speed, and  $V$  the chamber volume.

This equation may also be written for the chamber plus sample, where  $Q_s$  is the sample outgassing rate.

$$Q_P = Q_o + Q_s - \frac{V}{P} \left( \frac{dP}{dt} \right)_s \quad (10)$$

By subtraction at constant pressure

$$Q_s = \frac{V}{P} \left[ \left( \frac{dP}{dt} \right)_o - \left( \frac{dP}{dt} \right)_s \right] \quad (11)$$

Thus  $Q_s$  at a given pressure is proportional to the difference between the slope of the empty chamber and the chamber-plus-sample pump-down curves. It is not necessary to know the system pumping speed.

Pump-down tests consisted of determination of pump-down curves of the empty chamber, and of the chamber plus samples of Dexiglas, NRC single-aluminized Mylar, aluminum foil, and double-aluminized Mylar. Each sample had a face area of  $93,000 \text{ cm}^2$ . The pump-down curves were taken for a two-hour period. Figure 20 shows the pressure/time history for the samples in off-shelf condition. The test data for the second and third run of each sample are very similar to their initial test data in most cases.

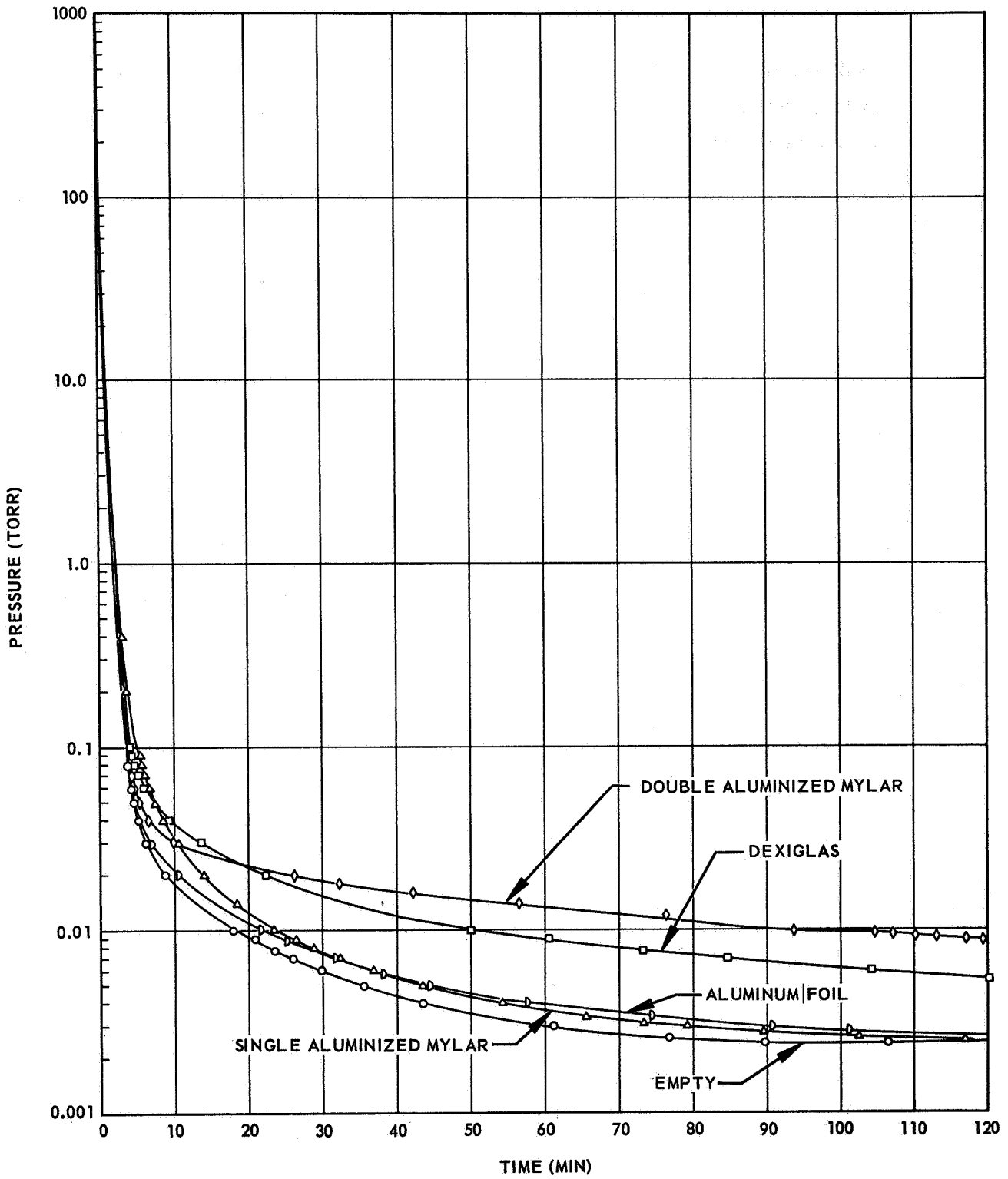


Fig. 20 Pump - Down Characteristics for Several Off-Shelf Insulation Materials

The raw experimental data are in the form of pressure and time points. The slope of the P - t curve between the nth point and the (n + 1)th point was found as follows:

$$\frac{1}{P} \frac{dP}{dt} = \left( \frac{2}{P_n + P_{n+1}} \right) \cdot \left( \frac{P_{n+1} - P_n}{t_{n+1} - t_n} \right) \quad (12)$$

where

$$P = \frac{P_n + P_{n+1}}{2} \quad (13)$$

These values of  $\frac{1}{P} \frac{dP}{dt}$  were plotted against P for each test and were smoothed graphically. Tables were then prepared from the smoothed  $\frac{1}{P} \frac{dP}{dt}$  versus P curves showing  $\frac{1}{P} \frac{dP}{dt}$  for each sample at constant pressure values. Using equation Q<sub>s</sub> could be found. The final data were prepared in the form of  $\left( \frac{PQ}{A} \right)$  values, where A is the sample area. This quantity, the outgassing rate in torr cm<sup>3</sup>/cm<sup>2</sup> min, can be plotted versus pressure or time, which has been done in Figure 21.

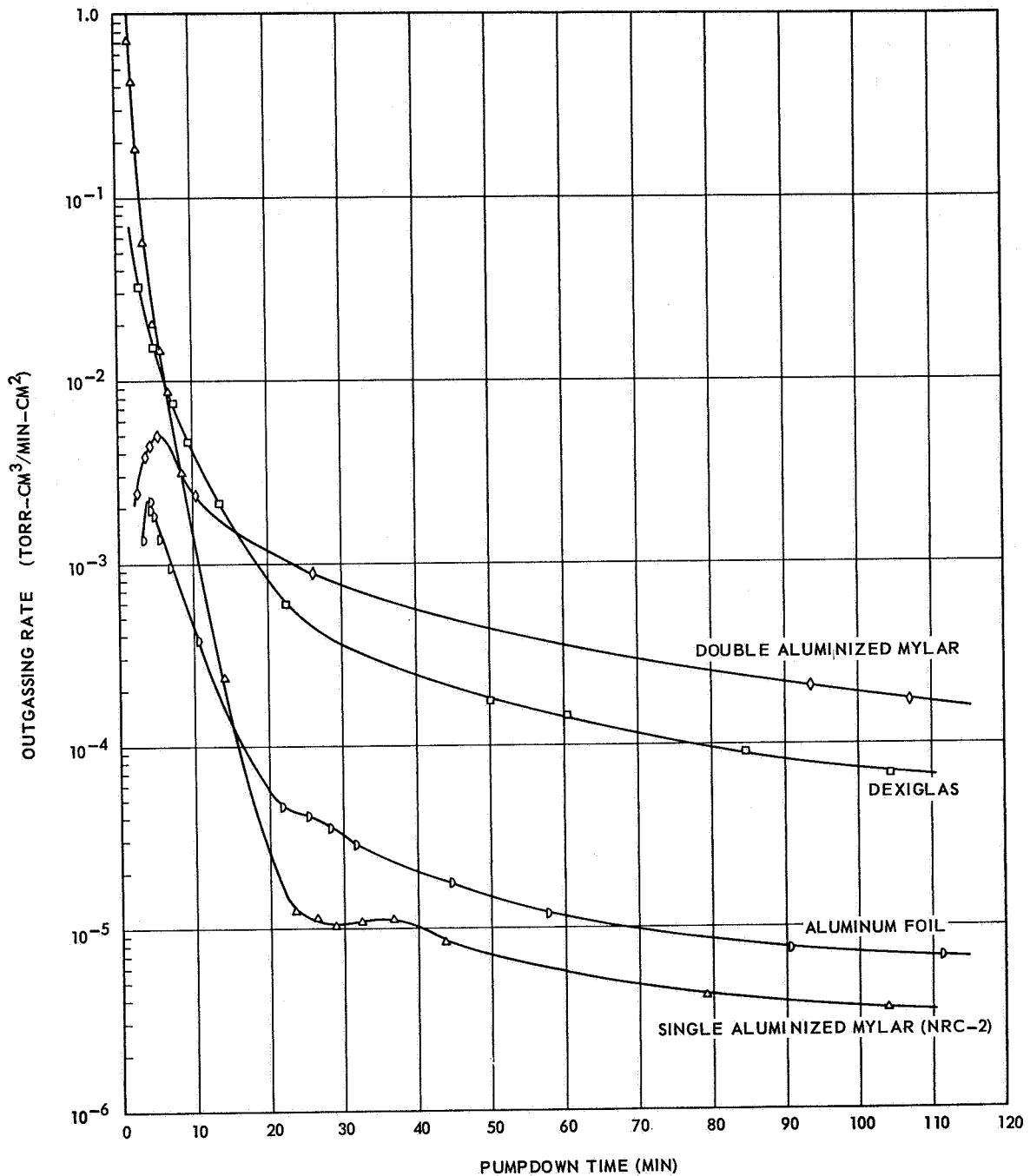


Fig. 21 Mass Outgassing Rate for Off-Shelf Samples of Multilayer Insulation Materials at Ambient Temperature

## TASK 2: DIFFUSION COEFFICIENT STUDY

The flowmeter described in the Second Quarterly Progress Report has been constructed and calibrated. Calibration involved the determination of certain simple geometric quantities such as tube areas and dead volumes. The meter has been checked out in conjunction with a vacuum system. This was accomplished by comparing steady-flow measurements given by each of the two upstream measuring valves, which have an area ratio of about ten. Reproducibility of measurements from an individual tube is better than  $\pm 1$  percent, while agreement between the results from different tubes is within about  $\pm 5$  percent.

The checkout tests were obtained using air. When helium was substituted for air very erratic readings were obtained. The degree of this behavior was reduced by taking greater pains to ensure that all the air dissolved in the meter oil had been removed and that helium was dissolved in the oil to an equilibrium value. Nevertheless, variations were still observed. It was supposed that this was due to the relative magnitude of the dissolved gas concentration relaxation time, the inherent slight variations in supply pressure, and the variation of helium concentration with pressure. The system relaxation time has been reduced by a factor of ten by filling up the interior of the flowmeter body with metal bar stock and lead shot. Tests are currently being tested to see if this modification has the desired effect.

The bleed valve from the flowmeter to the system used first consisted of a flattened copper tube about  $3/32$  in. in diameter wound into a  $1/4$ -in. diameter shaft. The tightness of this spiral could be varied by rotating one of its ends secured to the shaft, while the other end was held stationary. This valve worked well until a fatigue crack appeared. A new valve of the more conventional needle type has been ordered. In the meantime, preliminary testing is being continued using flat-seated valves.

A specimen of NRC-2 insulation, single-aluminized Mylar sheet has been wound onto the inner specimen drum of the diffusion apparatus. The resultant layer density is 67 layers/in. with a length of 36 in. The specimen has been fitted with a rigid outer skirt covering the entire length of the specimen so as to insure dimensional stability.

During the present reporting period several important changes have been made in the design of the diffusion apparatus. Previously, the container had been evacuated via a 4-in. diameter port in the bottom end. The vacuum line contained four elbows and was restricted by a 2-in. diameter shut-off valve. An untrapped 4-in. diffusion pump was used. Its pumping capacity of about 20 liters/sec was found to be insufficient. Recently another vacuum system became available which was adapted to the diffusion apparatus. This system utilizes a 6-in liquid-nitrogen trapped diffusion pump and has a 6-in. diameter screw-operated shut-off valve. The new pumping system has increased the effective pumping capacity by a factor of at least ten, from about 20 liters per sec to higher than 200 liters per sec.

Figures 22 and 23 show the modified diffusion apparatus. It is apparent that the modifications have been made only to the bottom end in order to adapt to the new pumping system. The opportunity was taken to incorporate Varian instead of Hughes ion gauge equipment so as to standardize with the Varian gauge at the upper end. Two gauges have been used at the bottom end; they have been positioned somewhat different so as to obtain some indication of the effect of gauge position on indicated pressure. This modification delayed the project by about one month due to the long delivery time. The diffusion apparatus modifications have been completed and initial test data obtained.

A pressure/time pump-down characteristic was determined for the 67-layer per in. sample of crinkled single-aluminized Mylar. This is shown in Figure 24. The pressure is that given by the Alphatron gauge on the upstream end of the sample (see Figure 22). The bleed line is closed off during this phase. The curve shows three distinct regions. The first shows the short period required to establish flow equilibrium after pump-down begins. The second represents steady-state continuum flow exhaustion. The third region, characterized by a change of slope, represents the slip and then free molecule flow regime. From the diagram the latter transition point is taken to be about 0.5 mm Hg, or about 1.4 lb/ft<sup>2</sup>. This compares favorably with a value of 2.78 lb/ft<sup>2</sup> given in Reference 2 for a sample of the 70 layer/in. aluminized Mylar interleaved with Dexiglas. This latter sample has in fact 140 material layers per in.; therefore, the interlayer distance is about half of that of the present NRC sample. Since the mean

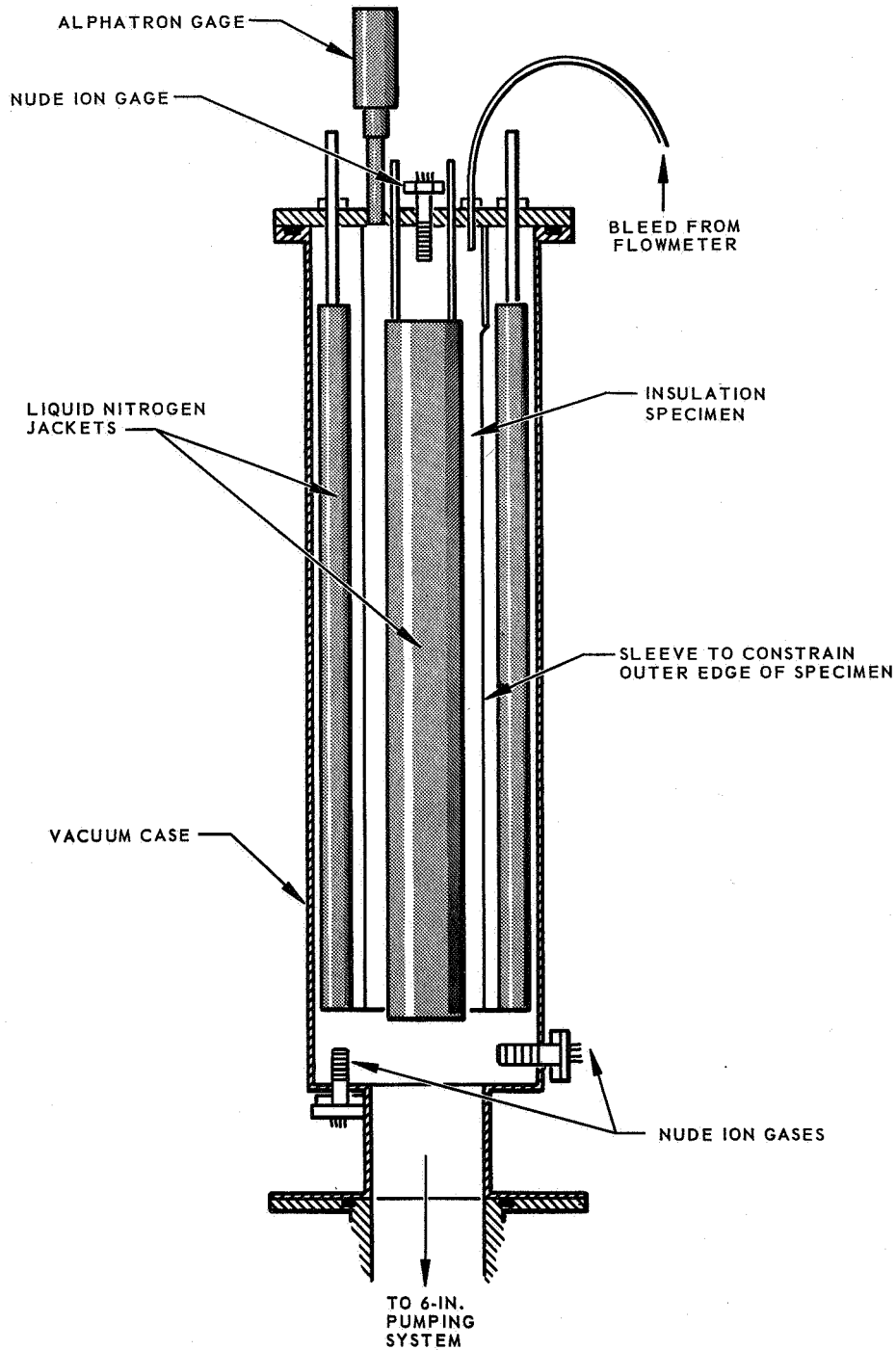


Fig. 22 Schematic of Diffusion Apparatus

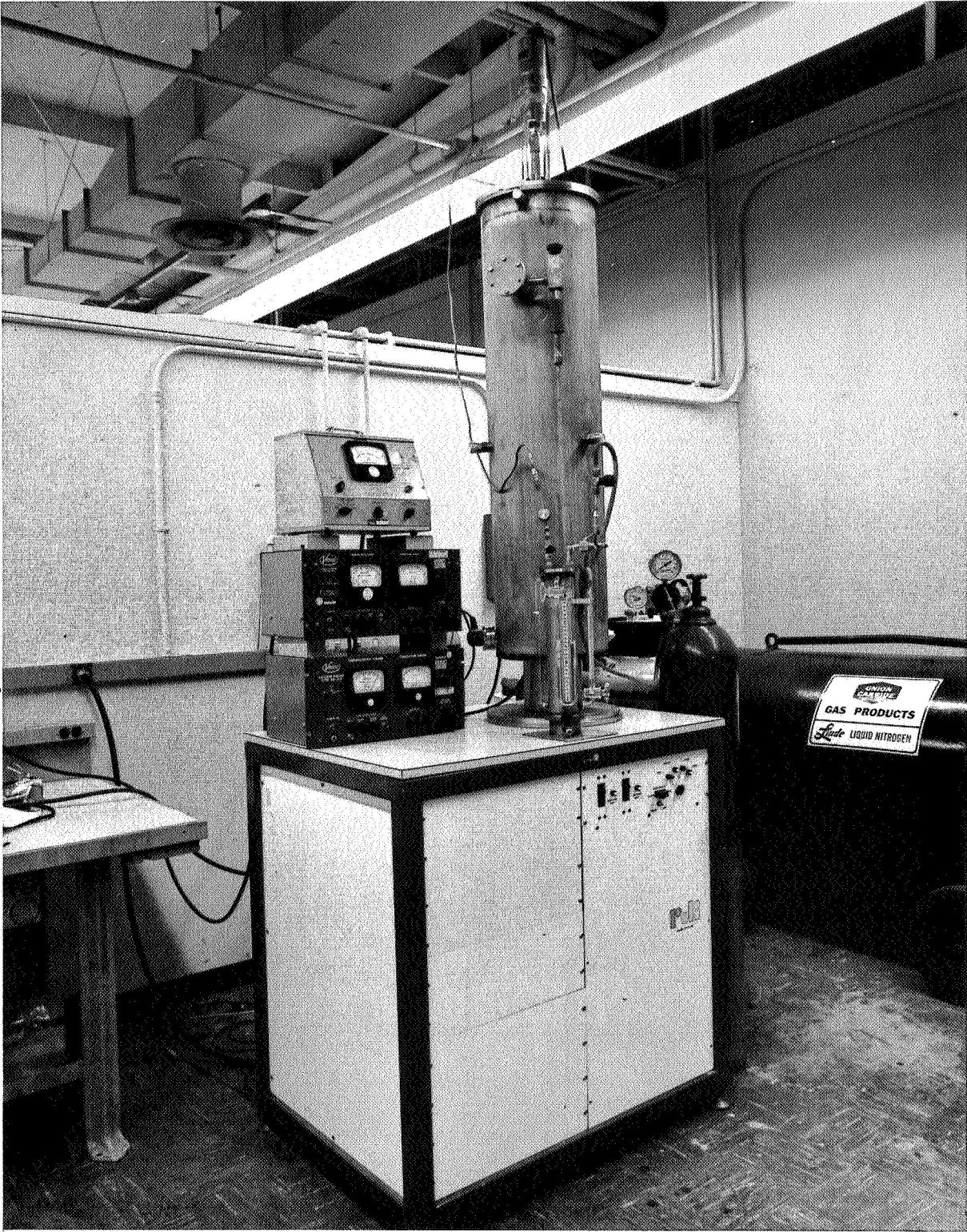


Fig. 23 Diffusion Apparatus

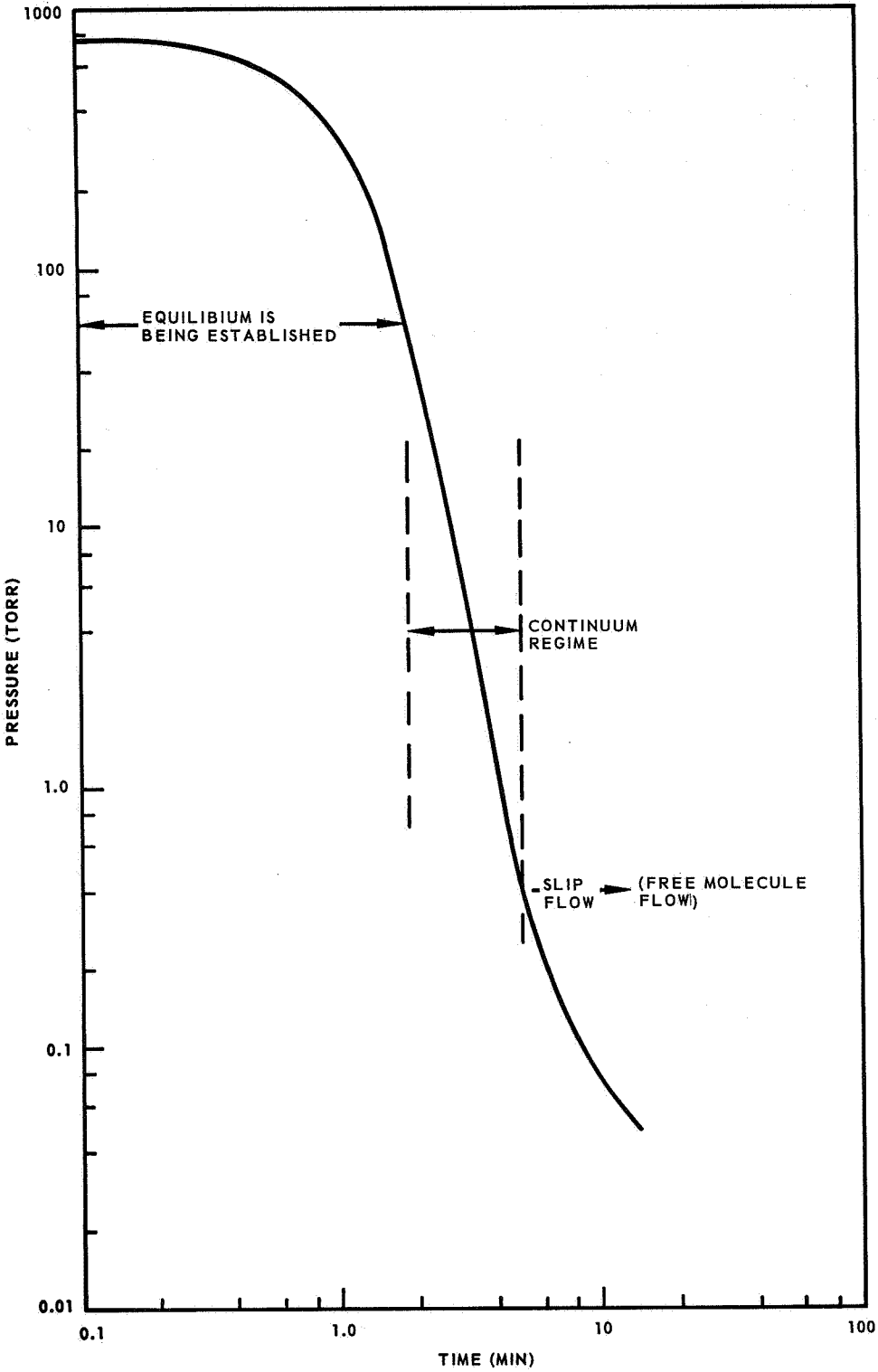


Fig. 24 Pump - Down Curve for NRC-2 Insulation Sample (Crinkled Single-Aluminized Mylar), 67 Layers/in.

free path of air is approximately inversely proportional to pressure, these two data compare favorably qualitatively. In other words, the experimentally determined ratio of mean free path to interlayer separation distance at the transition point is roughly the same in both cases.

With the present sample in the apparatus data will be taken at room temperature using air and helium to compare with the theoretical effect of molecular weight; then, using one gas data will be taken at three temperatures to compare with the theoretical effect of this variable. Then a range of insulation systems and wrapping densities will be tested at one temperature and with one gas.

## REFERENCES

1. Kittel, C., Introduction to Solid State Physics, John Wiley & Sons, Inc., New York
2. LMSC-A742593-V, "Analytical and Experimental Studies of Gas Flow Through Multi-layer Insulations," August 1965